POLITECNICO DI TORINO

Master's Degree in Ingegneria Aerospaziale

Master's Degree Thesis

Moon Transfer Design Using Weak Stability Boundary

Supervisors

Prof. Lorenzo CASALINO

Candidate

Federica BRASI

March 2022

Abstract

The aim of this work is to analyze the feasibility of Earth-Moon transfers using weak stability boundary, in order to reach a Halo orbit around L_2. The analysis is firstly conducted in the CR3BP (Circular Restricted 3 Body Problem) and afterwards perturbations are introduced.

The objective of such transfer is to reduce the mission cost by lowering the propellant requirements compared to a traditional Hohmann transfer, aiming for a ballistic capture at Moon arrival. Such capture is possible using a region in space in which the gravitation forces of the influencing bodies tend to balance each other, called weak stability boundary.

Firstly a suitable destination Halo orbit is computed using differential correction in a single shooting method, with an attention to the stability of the Halo orbit in order to reduce station keeping costs. Afterwards, with the aid of invariant manifolds, the trajectory connecting a circular low Earth orbit to the selected Halo is obtained in the CR3BP. Two trajectory are proposed, using weak stability boundaries around L_2 in the Earth-Moon system and around either L_1 or L_2 in the Sun-Earth system in order to achieve the required transfer. The analysis is conducted for different Moon phases at arrival.

Secondly perturbations to the baseline trajectory calculated are introduced and a perturbed trajectory is computed, using multiple-shooting method, considering a Moon arrival window of a year.

Lastly consideration on the effect of Moon phase are reported, followed by a comparison of the two transfer options in the CR3BP and the perturbed system, and on the variability of the transfer cost and time throughout an year. Finally some conclusive remarks on the convenience of such transfer and the reliability of the CR3BP model are presented.

Table of Contents

List of Tables

List of Figures

Chapter 1

Introduction

In this chapter an introduction to the problem in analysis and the theory utilised are presented. Additionally some examples of notable missions are underlined.

1.1 Hohmann Transfer

The Hohmann transfer was first described by Walter Hohmann, a German scientist, in 1925. It utilises an elliptical orbit to connect two circular orbits with different radius around a central body in the same plane. Two maneuvers are required, one at departing orbit and one upon arrival. An example of transfer is shown in figure 1.1. This maneuver is commonly used in space mission and is the base for the standard transfer to the Moon.

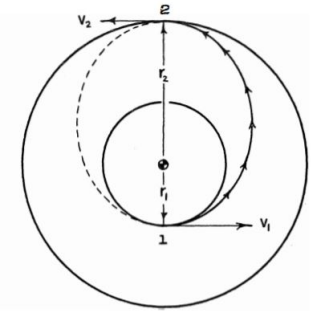

Figure 1.1: Example of Hohmann Transfer [1]

For Earth-Moon Hohmann transfer the second manoeuvre is used to adjust the velocity to the Moon velocity, therefore allowing capture. A ΔV different from zero is always required (around 1 km/s) in order to achieve capture at destination.

1.2 Low cost Transfer

Edward Belbruno in 1986 discovered a strategy to achieve ballistic capture, which is an automatic temporary capture at $\Delta V = 0$, therefore without the need for propulsion. A mathematical definition will be introduced in the following chapter (see 2.5). The method allows for temporary capture, but a permanent capture, if required, can be achieved with a extremely small ΔV, obtaining a big reduction in required fuel. Such transfer utilise, what he defines, weak stability boundaries.

1.2.1 Weak Stability Boundaries

A good explanation of weak stability boundaries in the Earth-Moon system can be found [2]: "Weak Stability Boundary (WSB) transfers are low energy transfers that take advantage of regions where the gravitational attraction of the influencing bodies tend to balance each other, to achieve ballistic capture at Moon". While different mathematical definitions where given throughout the years, the definitive one can be found in [3] and will be introduced in the following chapter (see 2.6).

1.2.2 Theory Development and Important Milestones

The possibility of a ballistic capture was first introduced in 1986 by Belbruno. The trajectory, utilised to achieve ballistic capture, was computed in the Earth-Moon three body problem (see 2.2) and was unable to reach low Earth orbit arriving at 60000 km from Earth center. The trajectory was created with solar electric engines as propulsive systems and was utilised in the 2003 SMART 1 mission by ESA. A representation can be found in figure 1.2.

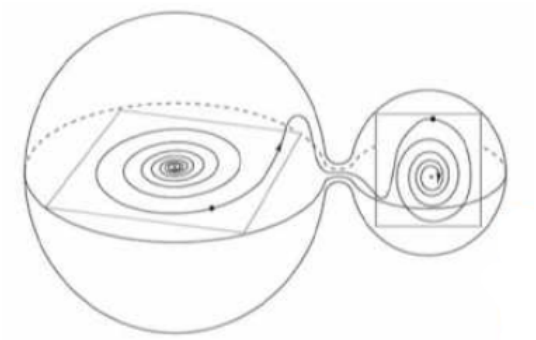

Figure 1.2: First Weak Stability Transfer [4]

Afterward in 1991, for the Japanese Hiten mission, Belbruno developed a second weak stability transfer in the four body problem, considering two weak stability boundaries: one in the Earth-Moon system and one in the Sun-Earth system.

During this study the role of invariant manifolds (see 2.3) was firstly underlined, but not utilized in trajectory calculation. The reference trajectory is reported in figure 1.3.

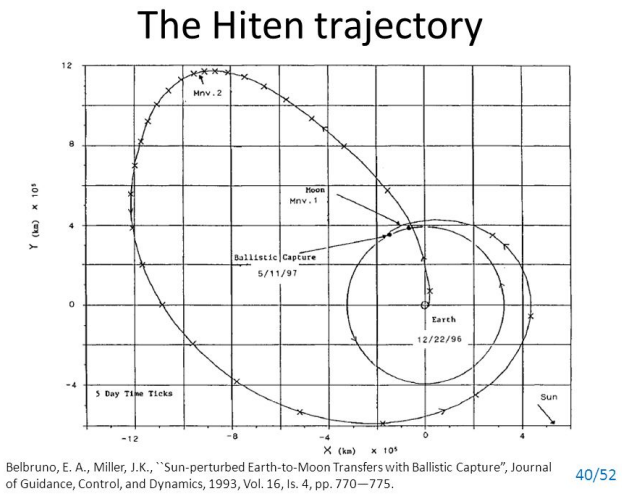

Figure 1.3: Hiten trajectory [5]

In 2007 Garcia and Gomez [6] wrote an important article in which they introduced a generalization of the algorithm developed by Belbruno, which included manifolds in the trajectory calculation, and allowed for an updated definition of weak stability boundaries, which is the one used today and will be presented in the following chapter (see 2.6).

1.2.3 Comparison with the Hohmann transfer

Trajectories in weak stability allow for a reduction in transfer cost, especially at moon arrival, with a slight increase in the cost for low Earth orbit departure (usually around 0.2 km/s) and a consistent increase in travel time, from days in the Hohmann transfer to months in weak stability transfers. In case of insertion into a low Moon orbit the predicted reduction in ΔV at Moon arrival is 25% compared to the Hohmann transfer. Weak stability transfer allows for direct transfer to halo orbits around L_2 in Earth-Moon system with even higher fuel saving compared to traditional solutions. This second option will be investigated in this analysis.

1.3 Notable Missions

In this section import mission that utilised weak stability transfers are presented.

1.3.1 SMART-1

SMART-1 was ESA's first Moon mission, launched in 2003 from Kourou, French Guiana. The objectives of the mission where to investigate the Moon, study chemical elements in the lunar surface, and to demonstrate the use of advanced ion propulsion for navigation and a number of innovative mission control techniques. It was the first European mission to utilise electric-ion propulsion. The trajectory was based on the developed by Belbruno in 1986, reported in figure 1.2. The mission was successful and the spacecraft completed its mission with a controlled impact with the Moon in 2006 [7].

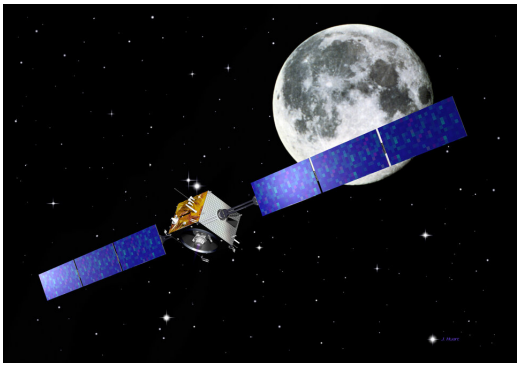

Figure 1.4: SMART-1 spacecraft [7]

1.3.2 HITEN

It was the first Japanese lunar mission and also the first robotic lunar probe since the flight of the Soviet Luna 24 in 1976. The objective of the two-module Japanese spacecraft was to fly past the Moon and release an orbiter. Due to a problem with the orbital injection burn, MUSES-A (Mu-launched Space Engineering Satellite), renamed Hiten ("musical angel") was released in a lower orbit than planed and, after a number of subsequent maneuvers, Hiten reached its originally planned nominal orbit. After the completion of its primary mission, which included the release of a "grandchild" satellite named Hagoromo and test aerobreaking into Earth's atmosphere for the first time by any spacecraft, Hiten began an unexpected extended mission to experiment with a novel method to enter lunar orbit utilising the second weak stability trajectory developed by Belbruno, represented in figure 1.3 [8].

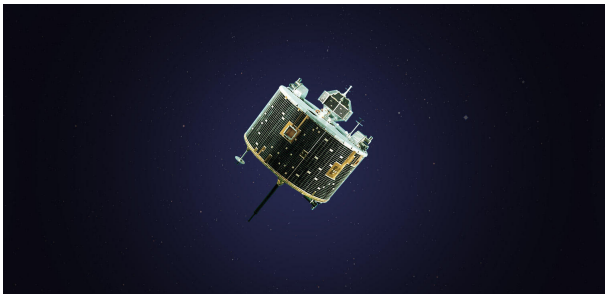

Figure 1.5: HITEN spacecraft [9]

1.3.3 GRAIL

The Gravity Recovery and Interior Laboratory, or GRAIL, mission was designed by NASA in order to create an accurate gravitational map of the Moon, which when combined with topographic data, can provide insight into the Moon's internal structure, composition and evolution. The twin spacecraft (Ebb and Flow) of NASA's GRAIL mission where launched in 2011 from Cape Canaveral and concluded their final rocket burns and impacted the Moon On December 17, 2012. NASA has named the site in honor of the late astronaut Sally K. Ride, who was America's first woman in space and a member of the probes' mission team. A low energy transfer was selected in order to reduce the propellant mass and the longer transfer time was beneficial to the mission since the on-board Ultra-Stable Oscillator needed to be continuously powered for several months in order to reach a stable operating temperature required for measurements [10].

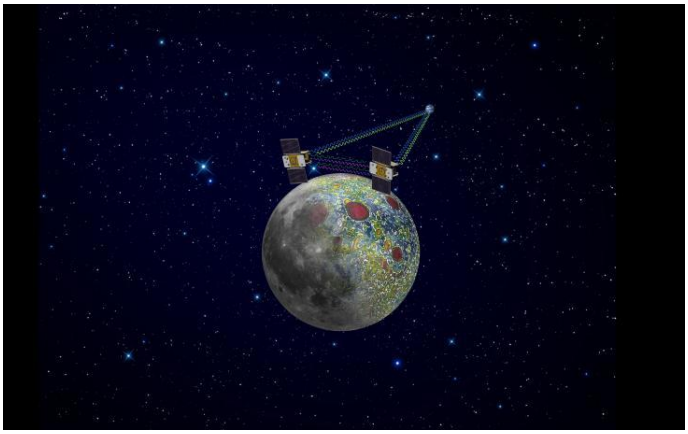

Figure 1.6: SMART-1 spacecraft [10]

1.4 Current interests

Part of NASA plan for the return to the Moon, the Artemis program, include a lunar station, Gateway, that will be an outpost orbiting the Moon that will provide vital support for a long-term human return to the lunar surface, as well as a staging point for deep space exploration. The station will orbit a Near-rectilinear halo orbit, a type of halo orbit.

Figure 1.7: Rendering of Gateway [11]

Chapter 2

Theoretical Notions

In this chapter theoretical notions applied in the analysis will be explained. The reference frame utilised for the first part of the analysis, CR3BP, will be presented, together with the equations of motion. Then libration points and notable orbits around such points are introduced, followed by some important tolls used: Manifolds and Poincarè section. Finally mathematical definition for ballistic capture and weak stability boundary, introduced in the previous chapter, is presented.

2.1 N-body problem

In order to describe the motion of a body, (i.e. a satellite, probe or celestial body) in space it is necessary to take into account, among other phenomena, the gravitational effect of surrounding bodies. Such problem can be modelled utilizing the N-body problem, which allows for the calculation of the total force excited on the probe by applying the Newton's law of universal gravitation (described in equation 2.1), which computes the attractive force between the bodies with masses m_i and m_j and distance vector between the bodies $\mathbf{r_{ij}}$ defines as in equation 2.2; while the system can be schematized as in figure 2.1.

$$\mathbf{F_{ij}} = -G\frac{m_i m_j}{{r_{ij}}^3}\mathbf{r_{ij}} \tag{2.1}$$

$$\mathbf{r_{ij}} = \mathbf{r_i} - \mathbf{r_j} \tag{2.2}$$

In a N-body problem the total force applied to the body of interest m_i is the sum of the forces applied by the other N-1 bodies (m_j with $j \neq i$) in the system, which, in summation notation, is explicated in equation 2.3.

$$\mathbf{F} = -G \sum_{j=1, j\neq i}^{N} \frac{m_i m_j}{r_{ij}^3}\mathbf{r_{ij}} \tag{2.3}$$

For a more complete analysis other components can be added, for example the solar radiation pressure, but will not be included in this work due to the additional complications. In many occasions the resolution of the N body problem, even considering only the gravitational effect, requires a high computational cost and reducing the number of bodies considered allows to discover interesting proprieties that can be afterward utilised in a complete force model with the appropriate corrections. Therefore, at the beginning of the analysis a simplified model in used: the three body problem.

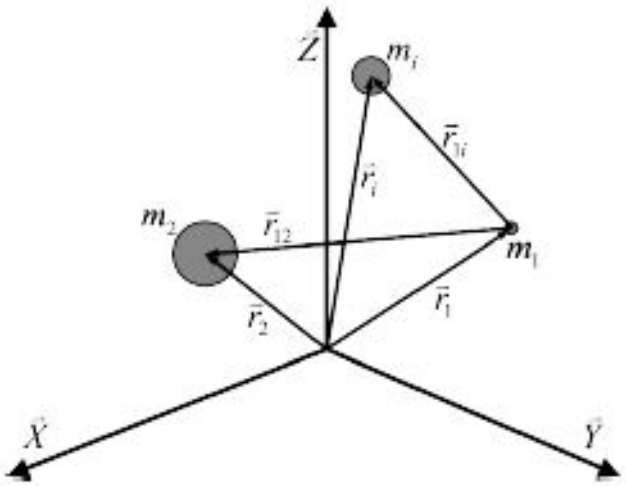

Figure 2.1: N-body model representation [12]

2.2 Three Body Problem

The three body problem is a simplification of the N-body-problem with includes a primary body m_1, a secondary body m_2 and a spacecraft (in general a body with negligible mass compared to the other two bodies, therefore unable to affect their motion). Furthermore, if the orbit of the two massive bodies, around their common center of mass, is considered circular, the problem is called circular restricted three body problem, usually referred as CR3BP. A schematic representation of the problem can be found in figure 2.2.

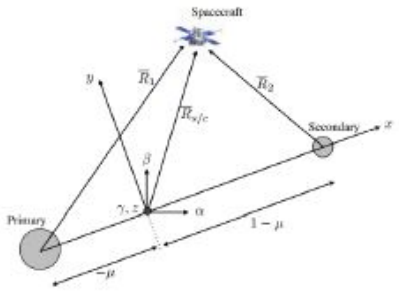

Figure 2.2: Three Body Problem [12]

2.2.1 Dimensionless Quantities

It is convenient to utilise dimensionless quantities in the analysis. Throughout the analysis the following conversion are used:

- distance $d' = Ld$
- velocity $s' = Vs$
- time $t' = \frac{T}{2\pi}t$.

The primed quantities are dimensional while the unprimed ones are dimensionless. L, V, T are the transformation parameters and correspond respectively: to the distance between the center of m_1 and m_2, to the orbital velocity of m_2 and to the orbital period of the system. By utilizing dimensionless quantities the only parameter of the system is the mass parameter which is described in equation 2.4.

$$\mu = \frac{m_2}{m_1 + m_2} \tag{2.4}$$

The mass parameters and transformation parameters uses in the following chapter as summarised in table 2.1.

System	μ	L [m]	V [km/s^2]	T [s]
Sun-Earth	$3.036 \cdot 10^{-6}$	$1.496 \cdot 10^5$	29.784	$3.147 \cdot 10^7$
Earth-Moon	$1.215 \cdot 10^{-2}$	$3.850 \cdot 10^5$	1.025	$2.361 \cdot 10^6$

Table 2.1: Mass parameters and dimensional values [13]

2.2.2 Inertial and Rotating Reference System

For simplicity, the problem is usually described in a rotating reference system, as described in the figure 2.3a. The relation between inertial and rotating reference systems is illustrated in figure 2.3b. Where the capitol letters indicate the inertial reference system and the lower case letters the rotating system.

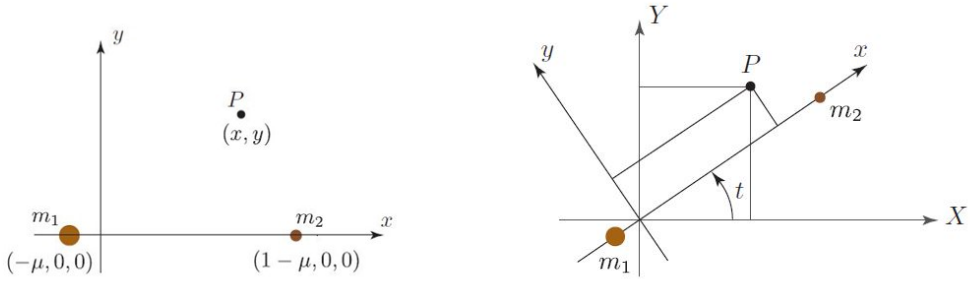

(a) Rotating frame [13]

(b) Inertial and Rotating frames [13]

Figure 2.3: Rotating frame and comparison with inertial [13]

Assuming the two reference frame coincide at $t = 0$, transformation between the two reference frames can be achieved as in equation 2.5, where A_t is as in equation 2.6.

$$\begin{pmatrix} X \\ Y \\ Z \end{pmatrix} = A_t \begin{pmatrix} x \\ y \\ z \end{pmatrix} \tag{2.5}$$

$$A_t = \begin{bmatrix} \cos t & -\sin t & 0 \\ \sin t & \cos t & 0 \\ 0 & 0 & 1 \end{bmatrix} \tag{2.6}$$

Also the velocity components can be transformed deriving equation 2.5. Results are reported in equation 2.7

$$\begin{pmatrix} \dot{X} \\ \dot{Y} \\ \dot{Z} \end{pmatrix} = \dot{A}_t \begin{pmatrix} x \\ y \\ z \end{pmatrix} A_t \begin{pmatrix} \dot{x} \\ \dot{y} \\ \dot{z} \end{pmatrix} \tag{2.7}$$

2.2.3 Equations of Motion in Inertial Reference System

The equations of motion in the inertial reference frame can be found in equation 2.8. U_x, U_y, U_z are partial derivatives of the pseudopotential U defined in equation

2.9, where r_1 and r_2 are the position of the spacecraft relative, respectively, to the primary and secondary body, and are defined in equation 2.10 and 2.11.

$$\begin{aligned} \ddot{x} &= -U_x \\ \ddot{y} &= -U_y \\ \ddot{z} &= -U_z \end{aligned} \tag{2.8}$$

$$U = -\frac{1-\mu}{r_1} - \frac{\mu}{r_2} - \frac{1}{2}\mu(1-\mu) \tag{2.9}$$

$$r_1 = \sqrt{(X+\mu\cos t)^2 + (Y+\mu\sin t)^2 + Z^2} \tag{2.10}$$

$$r_2 = \sqrt{(X-(1-\mu)\cos t)^2 + (Y-(1-\mu)\sin t)^2 + Z^2} \tag{2.11}$$

The pseoudopotential is a measure of the potential energy of the system and it is always less than zero. Therefore to avoid dealing with negative numbers it is common practise to define energy levels utilising the Jacobi integral C as in equation 2.12.

$$C(x,y,z,\dot{x},\dot{y},\dot{z}) = -(\dot{x}^2+\dot{y}^2+\dot{z}^2) - 2U \tag{2.12}$$

2.2.4 Equations of Motion in Rotating Reference Frame

The equations of motion derived for the inertial reference frame 2.8 can be transformed in the rotating reference system utilising the Euler-Lagrange equation (2.13). Where L is the lagrangian (i.e the difference between the cinetic and potential energy). For the inertial system the lagrangian ($\mathcal{L}$) in reported in equation 2.14, while in the rotating system 2.15 .

$$\frac{d}{dt}\frac{\partial L}{\partial \dot{q}^i} - \frac{\partial L}{\partial q^i} = 0 \tag{2.13}$$

$$\mathcal{L}(X,Y,Z,\dot{X},\dot{Y},\dot{Z},t = \frac{1}{2}(\dot{X}^2+\dot{Y}^2+\dot{Z}^2) - U(X,Y,Z,t) \tag{2.14}$$

$$L(x,y,z,\dot{x},\dot{y},\dot{z}) = \frac{1}{2}((\dot{x}-y)^2+(\dot{y}+x)^2+\dot{z}^2) - U(x,y,z) \tag{2.15}$$

In the rotation system the lagrangian (L) is time independent and is obtained rewriting the kinetic and potential energy of the inertial frame Lagrangian $\mathcal{L}$ in rotating coordinates. For the kinetic energy equation 2.7 is required, while, since distances are invariant under rotation the pseudopotential maintains the same formulation, with different expression for r_1 and r_2, defined in equation 2.16 and 2.17.

$$r_1 = \sqrt{(x+\mu)^2 + y^2 + z^2} \tag{2.16}$$

$$r_2 = \sqrt{(x-1+\mu)^2 + y^2 + z^2} \tag{2.17}$$

The Euler-Lagrange equation can be obtained for the present case as 2.18. After simplification the equations of motion in the rotating reference frame (in the future refereed simply as equations of motion) can be found in equation 2.19.

$$\begin{aligned} \frac{d}{dt}(\dot{x} - y) &= \dot{y} + x - U_x \\ \frac{d}{dt}(\dot{y} + x) &= -(\dot{x} - y) - U_y \\ \frac{d}{dt}\dot{z} &= -U_z \end{aligned} \tag{2.18}$$

$$\begin{aligned} \ddot{x} &= 2\dot{y} - U_x \\ \ddot{y} &= -2\dot{x} - U_y \\ \ddot{z} &= -U_z \end{aligned} \tag{2.19}$$

Substituting (2.19) in (2.9) equations 2.20 are obtained:

$$\begin{aligned} \ddot{x} &= 2\dot{y} - (1-\mu)\frac{x+\mu}{r_1^3} - \mu\frac{x-1+\mu}{r_2^3} \\ \ddot{y} &= -2\dot{x} - (1-\mu)\frac{y}{r_1^3} - \mu\frac{y}{r_2^3} \\ \ddot{z} &= -(1-\mu)\frac{z}{r_1^3} - \mu\frac{z}{r_2^3} \end{aligned} \tag{2.20}$$

2.2.5 Libration Points

In the CR3BP it is possible to identify five equilibrium points, known as libration points o Lagrangian points, where the gravitational forces acting on the third body balance each other. By definition, in the equilibrium point the velocity components in equation 2.20 are equal to zeros. The equilibrium point are therefore positioned in the x-y plane and are obtained by solving equations 2.21.

$$\begin{aligned} x - (1-\mu)\frac{x+\mu}{r_1^3} - \mu\frac{x-1+\mu}{r_2^3} &= 0 \\ y - (1-\mu)\frac{y}{r_1^3} - \mu\frac{y}{r_2^3} &= 0 \end{aligned} \tag{2.21}$$

By solving the second of the equations 2.21 the 3 collinear points are fond (L_1, L_2, L_3) and by solving the two equations coupled the saddle points are fond (L_4 and L_5). Their spatial location can be visualised in figure 2.4. Each equilibrium

point has a particular energy level. The energy level determines the real of possible motion of the spacecraft, defined as Hill's region. Five basic configurations (figure 2.5) for the Hill's region can be found comparing the spacecraft and the equilibrium points energy. The energy of the spacecraft is therefore a measure of how far it can travel and will be important in the trajectory definition.

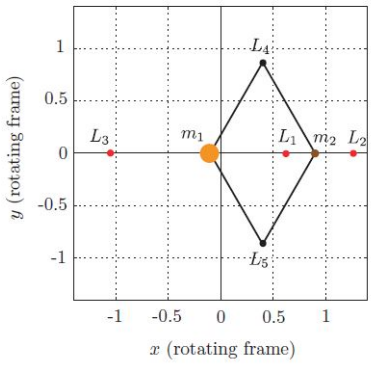

Figure 2.4: Libration Points [13]

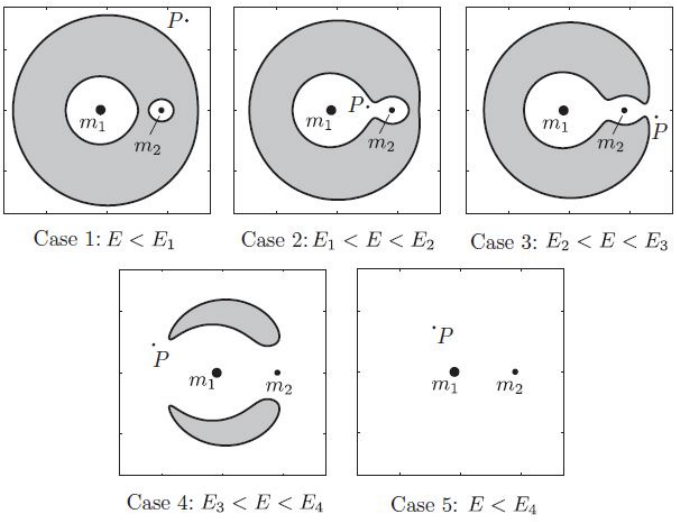

Figure 2.5: Hill's Region: P *represents the spacecraft, the inaccessible region is in grey* [13]

2.2.6 Motion near Collinear Equilibrium Points

Equations of motion can be developed using Legendre polynomials P_n. The existence of periodic solutions to the nonlinear equation can be deduced using the linear part of such equations, reported in 2.22, with c_2 defined as 2.23 and γ the normalised distance between the equilibrium point and the secondary body (e.g. γ_1 in Sun- Earth system is equal to 1.001090475 10^{-2} and is the normalised distance between Earth and L_1).

$$\begin{aligned} \ddot{x} - 2\dot{y} - (1 - 2c_2)x = 0 \\ \ddot{y} - 2\dot{x} + (c_2 - 1)y = 0 \\ \ddot{z} + c_2 z = 0 \end{aligned} \tag{2.22}$$

$$\begin{aligned} c2 = \frac{1}{\gamma_1^3}\left[\mu + (1-\mu)\frac{\gamma_1^3}{(1-\gamma_1)^3}\right] \quad \text{for} L_1, \\ c2 = \frac{1}{\gamma_2^3}\left[\mu + (1-\mu)\frac{\gamma_2^3}{(1-\gamma_2)^3}\right] \quad \text{for} L_2 \\ \ddot{z} + c_2 z = 0 \end{aligned} \tag{2.23}$$

The eigenvalues of the system are: $\pm\lambda$, $\pm i\omega_p$ known as planar frequency, $\pm i\omega_v$, known as vertical frequency, reported in 2.24.

$$\begin{aligned} \lambda^2 &= \frac{c_2 - 2 + \sqrt{9c_2^2 - 8c_2}}{2} \\ \omega_p^2 &= \frac{2 - c_2 + \sqrt{9c_2^2 - 8c_2}}{2} \\ \omega_v^2 &= c_2 \end{aligned} \tag{2.24}$$

If the initial conditions are restricted so that only the non-divergent mode is allowed the linearized equations have solutions of the form reported in 2.25, with κ as in equation 2.26.

$$\begin{aligned} x &= -A_x \cos(\omega_p t + \phi) \\ y &= \kappa A_x \sin(\omega_p t + \phi) \\ z &= A_z \sin(\omega_v t + \psi) \end{aligned} \tag{2.25}$$

$$\kappa = \frac{\omega_p^2 + 1 + 2c_2}{2\omega_p} \tag{2.26}$$

The linearized motion will become quasi-periodic if the in-plane and out-of-plane frequencies are such that their ratio is irrational. A simple example can be found imposing $\omega_p = \omega_v$. Different types of periodic or quasi-periodic orbits can be identified:

- Planar and Vertical Lyapunov orbits: which in limit have frequencies related to both ω_p and ω_v. Both are periodic orbits that lie entirely in the plane of the two primary bodies.
- Halo orbits: 3D periodic orbits (i.e. with an out of plane component not equal to zero). They appear in two families, northern and southern, symmetric with respect to the $z = 0$ plane.
- Lissajous, quasi-periodic 3D orbits in between Lyapunov and Halo orbits
- Quasi-Halo orbits: quasi-periodic orbits around the halo orbits.

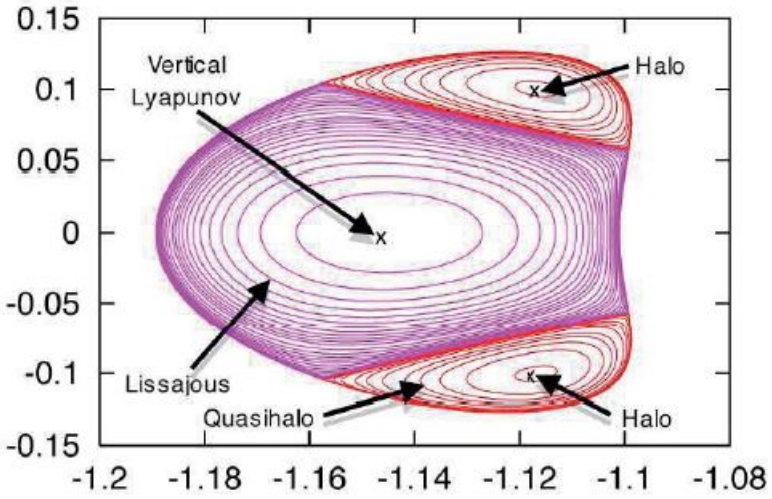

Figure 2.6: Poincarè section (see 2.4) at $z = 0$ corresponding to the L_2 point of the Earth-Moon system for $C = 3.142003$ [14]

2.3 Invariant Manifolds

2.3.1 Practical Definition

Manifolds are wildly used in different sectors from mechatronics to space trajectory. In the space sector they are used to compute trajectory connecting bodies with little to no use of propellant. In a simplistic way they can be defined as "tubes" that allow low cost connections between region of space, in particular near equilibrium points. Manifolds are directional and they depart or reach a halo orbit. If they depart from a halo orbit they are defined as unstable manifolds, while if they reach

a halo as stable manifolds. An example is presented in figure 2.7.

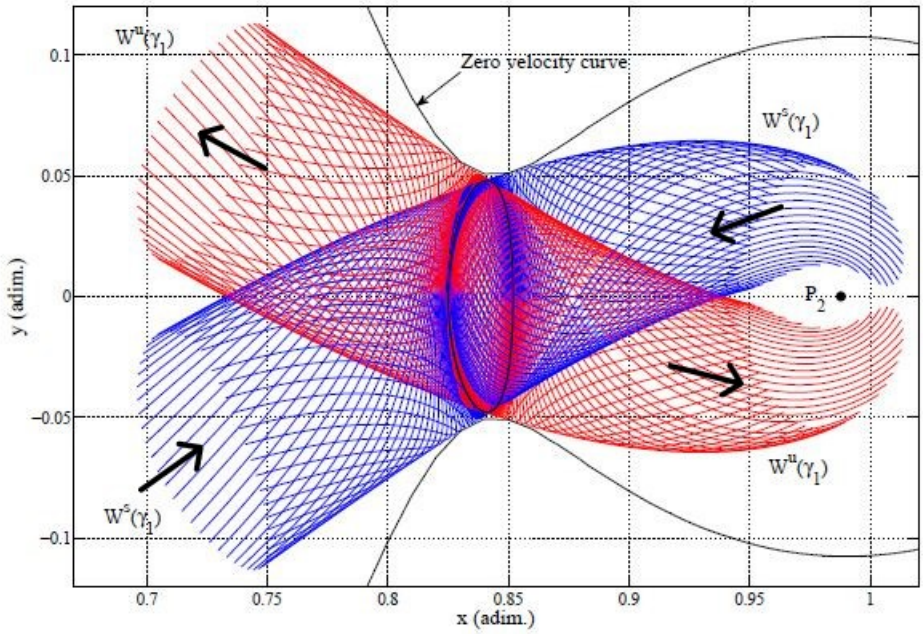

Figure 2.7: Example of Manifolds: *The stable manifold is represented in blue, the unstable manifold in red and the halo orbit in black [15]*

Manifolds could be considered as separators between possible trajectories. A brief description of the different case will now be presented in case of stable manifolds using as reference figure 2.7. Trajectories can follow:

- The interior of the manifolds
  In such case, if the spacecraft starts from the left side, it can enter the region of space near the secondary body, or if the spacecraft starts from the right side (i.e near the secondary body), it can depart from the body.

- The surface of the manifolds
  In such case, starting from each direction, the spacecraft reaches the halo orbit.

- The exterior of the manifolds
  In such case the spacecraft is unable to reach the halo which acts as a barrier impeding the passage from left to right or vice-versa. An example is presented in figure 2.8.

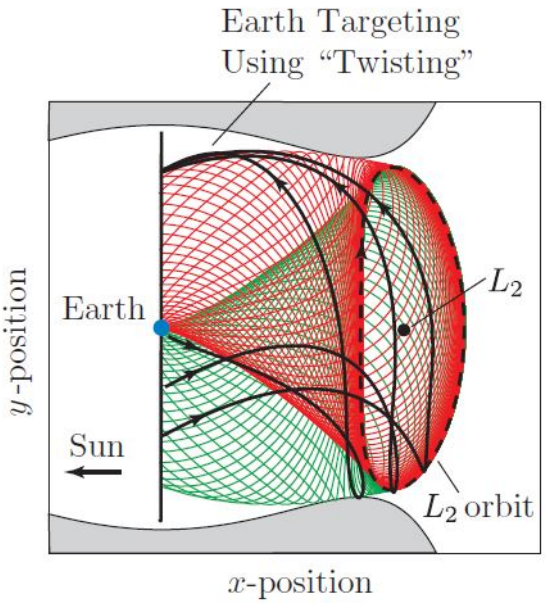

Figure 2.8: Example of Trajectory outside of Manifolds [13]

The description is analogue in case of unstable manifolds after taking into account the opposite directionality.

2.3.2 Mathematical Background

Some basic definitions are now provided, but for more advanced theoretical notions and rigorous mathematical definitions see [6].

Manifolds can be seen as an extension to higher dimensional systems of separatrices in planar systems (i.e. boundary separating two modes of behaviour in a differential equation), as shown in the previous section. Additionally the can be seen as a way to extend the stability characterization of linear systems to nonlinear ones.

Basic Notion of Stability Theory in Linear System

The stability of a generic linear system, as in equation 2.27, can be defined knowing eigenvalues ($\lambda_j = a_j + ib_j$) and eigenvectors ($E(\lambda_j)$) of the matrix A.

$$\dot{\mathbf{x}} = A\mathbf{x} \tag{2.27}$$

Eigenvectors define stable (E^s), unstable (E^u) and center (E^c) subspace of the matrix A. The stable subspace is defined by the eigenvectors whose corresponding eigenvalue has real part greater than zero ($a_j > 0$). Contrary the unstable subspace is defined by the eigenvectors whose corresponding eigenvalue has real part less than zero ($a_j < 0$). Finally the center subspace is defined by the eigenvectors whose corresponding eigenvalue has real part equal to zero ($a_j = 0$)

Basic Definition of Manifolds [16]

A k-manifold is a subset $S \subset \mathbb{R}^n$ that can be locally represented as the graph of a smooth function defined on a k-dimensional affine subspace of $\mathbb{R}^n$. As in the calculus of graphs, k manifolds have well defined tangent spaces at each point and these are independent of how the manifolds are represented (or parametrized) as graphs.

A k-manifold $S \subset \mathbb{R}^n$ is said to be invariant under the flow of a vector field $\mathbf{X}$ if for $x \in S$, $F_t(x) \in S$ for small $t > 0$, where $F_t(x)$ is the flow of $\mathbf{X}$. One can show that this is equivalent to the condition that X is tangent to S. One can thus say that an invariant manifold is a union of (segments of) integral curves of X.

Firstly a definition on invariant manifolds associated with a fixed point x_e, correspond to the origin for a linear system, is presented and then extended to invariant sets, such as period orbits. In a neighborhood of x_e, the tangent spaces to the stable, center, and unstable manifolds are provided by the generalized eigenspaces E^s, E^c, and E^u of the linearization $A = DX(x_e)$. For simplicity an hyperbolic point (i.e. point where the linearization has no center subspace) is selected. The dimension of the stable subspace be denoted k.

Theorem (Local Invariant Manifold Theorem for Hyperbolic Points). *Assume that* $\mathbf{X}$ *is a smooth vector field on* $\mathbb{R}^n$ *and that* x_e *is a hyperbolic equilibrium point. There is a* k*- manifold* $W_s(x_e)$ *and a* nk *manifold* $W_u(x_e)$ *each containing the point* x_e *such that the following hold:*

i *Each of* $W_s(x_e)$ *and* $W_u(x_e)$ *is locally invariant under* $\mathbf{X}$ *and contains* x_e*.*

ii *The tangent space to* $W_s(x_e)$ *at* x_e *is* E^s *and the tangent space to* $W_u(x_e)$ *at* x_e *is* E^u*.*

iii *If* $x \in W_s(x_e)$*, then the integral curve with initial condition* x *tends to* x_e *as* $t \to \infty$ *and if* $x \in W_u(x_e)$*, then the integral curve with initial condition* x *tends to* x_e *as* $t \to -\infty$

iv *The manifolds $W_s(xe)$ and $W_u(xe)$ are (locally) uniquely; they are determined by the preceding conditions.*

A graphic representation can be seen in figure 2.9. This theorem can be extended to non hyperbolic points and is called Global Stable Manifold Theorem of Sample.

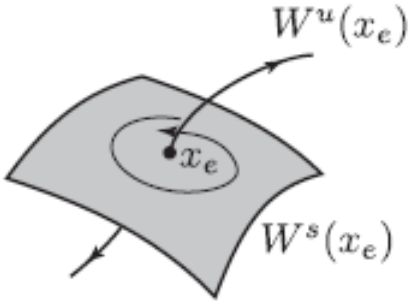

Figure 2.9: stable and unstable manifolds of a critical point with one eigenvalue of the linearization [15]

Similar results can be obtained for invariant manifolds of periodic orbits. A graphic representation is shown in figure 2.10.

Figure 2.10: stable and unstable manifolds of a periodic orbit [15]

2.4 Poincaré Section

The Poincaré section, named after Henri Poincaré, given a N dimensional space, is a lower-dimensional subspace transversal to the flow of the system. The intersection between a period orbit in the N dimensional space and the Poincaré section is defined as Poincaré map. An example is presented in figure 2.11.

Poincaré sections will be utilised in the analysis to compute the manifolds intersection. The position can be arbitrary as long as it respect the definition requirements. The case in analysis in 3-dimensional and therefore the poicare section will be a plane. For simplicity a Poincaré section with x coordinate coinciding with Earth position parallel to the $y - z$ plane in the Sun-Earth CR3BP is utilised. Further information and numerical demonstration can be found in [17].

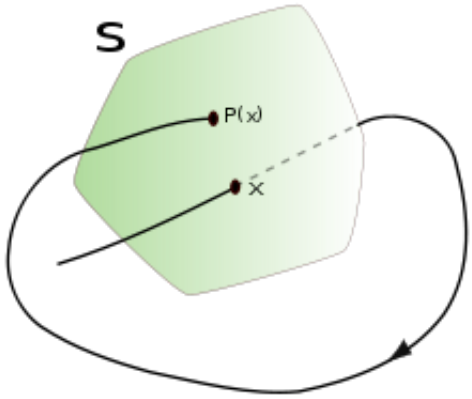

Figure 2.11: Poincare Map [18]

2.5 Ballistic Capture

In a three body problem a body of negligible mass (i.e. spacecraft), called P_3, is ballistically captured at time t_1 by a secondary body (P_2) if its Kepler energy is less than zero at t_1. And it is temporary ballistically captured (or weak captured) if its Kepler energy is less than zero for $t_1 \leqslant t \leqslant t_2$ and more than zero for $t < t_1$ and $t > t_2$, with t_1 and t_2 finite times and $t_1 < t_2$ [3]. Definition of Kepler energy is reported in equation 2.28, with μ gravitational parameter relative to a body, v velocity in km/s relative to inertial reference frame centered in the same body and r position vector relative to the same body in km.

$$E = \frac{v^2}{2} - \frac{\mu}{r} \tag{2.28}$$

2.6 Weak Stability Boundary

The region in which weak capture can occur is defined as weak stability boundary. In order to define such region trajectories of P_3 with the following initial conditions

will be considered:

- The initial position of the trajectory is on a radial segment $l(\theta)$ departing from P_2 and making an angle θ with the line connection primary (P_1) and secondary body (P_2), relative to the rotating system. The trajectory is assumed to start at the periapsis of an osculating ellipse around P_2, whose semi-major axis lies on $l(\theta)$ and whose eccentricity e is held fixed along $l(\theta)$.
- The initial velocity of the trajectory is perpendicular to $l(\theta)$, and the Kepler energy E of P_3 relative to P_2 is negative. The motion, for fixed values of the parameters θ and e, and for a choice of direction of the initial velocity vector such that a prograde osculating ellipse is achieved, depends only on the initial distance r.
- The motion is said to be n-stable if the infinitesimal mass P_3 leaves $l(\theta)$, makes n complete turns about P_2, and returns to $l(\theta)$ at a point with negative Kepler energy with respect to P_2, without making a complete turn around P_1 along this trajectory. The motion is otherwise said to be n-unstable. A visual representation can be found in figure 2.12.

Therefore the motion of P_3 is unstable either if P_3 performs a full circle about P_2 and returns to $l(\theta)$ with Kepler energy more then one (i.e P_3 performs a ballistic escape) or if P_3 moves away from P_2 and performs a full circle about P_1.

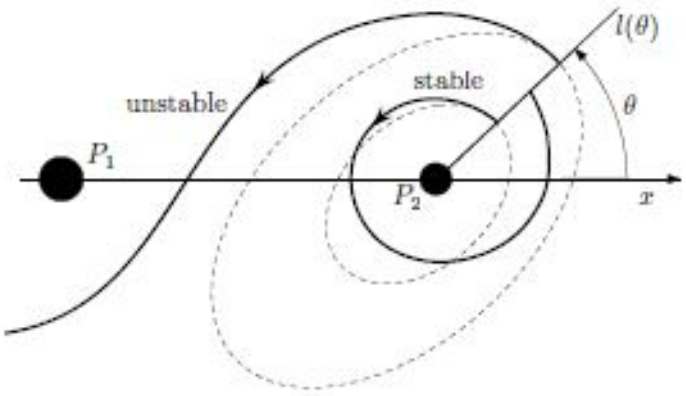

Figure 2.12: Example of 1-stable and unstable trajectories relative to P_2 [3]

The n-stability condition is an open condition, therefore the set of n-stable points on $l(\theta)$ is an open subset of $l(\theta)$, hence a countable union of open intervals as in equation 2.29.

$$W_n(\theta, e) = \bigcup_{k \geqslant 1} (r^*_{2k-1}, r^*_{2k}) \tag{2.29}$$

The weak stability boundary of order n, denoted by ∂W_n, can be defined as the locus of all points $r^*(\theta, e)$ along the radial segment $l(\theta)$ for which there is a change of stability of the initial trajectory, that is, $r^*(\theta, e)$ is one of the endpoints of an interval (r^*_{2k1}, r^*_{2k}) characterized by the fact that for all $r \in (r^*_{2k1}, r^*_{2k})$ the motion is n-stable, and there exist $r \notin (r^*_{2k1}, r^{2k)}$, arbitrarily close to either r^*_{2k1} or r^*_{2k} for which the motion is n-unstable. The set notation of ∂W_n is reporter in equation 2.30.

$$\partial W_n = \{r^*(\theta, e)|\ \theta \in [0,2\pi], e \in [0,1)\} \tag{2.30}$$

Chapter 3

Numerical Methods

In this chapter useful and recurring numerical methods utilised in the analysis are presented, in particular: differential correction, multi-variable Newton method. Furthermore a brief description of the integration specification of the differential equations is provided.

3.1 Differential Correction

Differential correction is a numerical method used to modify the initial condition of a problem in order to obtain, after a numerical integration, a desired final condition. It is best described as a process of targeting. Lets suppose the equations of motion of the system are described by a differential equation 3.1, where $\mathbf{x}$ represents the state vector, which include position and velocity coordinates.

$$\dot{\mathbf{x}} = f(\mathbf{x}) \tag{3.1}$$

A generic trajectory originating in $\mathbf{x_0}$ propagated for a time t can be written as $\phi(t, t_0) : \mathbf{x}(t_0) \rightarrow \mathbf{x}(t)$. In other words $\phi(t, t_0) : \mathbf{x}(t_0) \rightarrow \mathbf{x}(t)$ denotes the flow map of the dynamical system, mapping particles from their initial locationat time t_0 to their location at time t. In the future, for brevity, the flow map will be denoted as $\phi(t; \mathbf{x_0})$. It can be easily verified that the flow map satisfied the equations of motion 3.1.

$$\frac{d\phi(t; \mathbf{x_0})}{dt} = f(\phi(t; \mathbf{x_0})) \qquad \text{with} \quad \phi(t_0, \mathbf{x_0}) = \mathbf{x_0}$$

If a perturbation to the initial condition is introduced ($\mathbf{x_0} + \delta\mathbf{x_0}$) the displacement at a time t_1 can be described, utilising the flow map, as in equation 3.2. Which expanded in in Taylor series yields equation 3.3.

$$\delta\mathbf{x}(t_1) = \phi(t_1, \mathbf{x_0} + \delta\mathbf{x_0}) - \phi(t_1; \mathbf{x_0}) \tag{3.2}$$

$$\delta\mathbf{x}(t_1) = \frac{d\phi(t_1;\mathbf{x_0})}{d\mathbf{x_0}}\delta\mathbf{x_0} + \text{higher order terms} \tag{3.3}$$

Neglecting higher order terms, the matrix which satisfies equation 3.3 to fist-order is called state transition matrix (STM, for brevity) and usually abbreviated as $\Phi(t_1, t_0)$. This matrix gives the linear relationship between initial and final displacements as in equation 3.4.

$$\delta\mathbf{x}(t_1) = \Phi(t_1, t_0)\delta\mathbf{x_0} \tag{3.4}$$

The STM can also be seen as the solution to the variational equation 3.5, which is a linearised differential equation that describes the evolution in time of the $\delta\mathbf{x}$ variations. $A(\mathbf{x}(t))$ is the Jacobian matrix (i.e. matrix of all its first-order partial derivatives) of the flow field f evaluated along the reference trajectory.

$$\delta\dot{\mathbf{x}}(t) = A(\mathbf{x}(t))\delta\mathbf{x} \tag{3.5}$$

Lets imagine a desired final state vector: $\mathbf{x}_d = \mathbf{x}(t_f)$ and first guess initial condition $\mathbf{x_0} = \mathbf{x}(t_0)$. The initial condition needs to be modified in order to obtain, after a numerical integration of the system differential equations, the final condition desired. Without any adjustment the solution of the integration is, in general, equal to $\mathbf{x_1} = \mathbf{x_d} - \delta\mathbf{x_1}$. Knowing the $\delta\mathbf{x_1}$ and utilising equation 3.4 a suitable $\delta\mathbf{x_0}$ can be found and the initial condition modified. The process in repeated iteratively till $\delta\mathbf{x_1}$ is within a desired tolerance.

In order to apply differential correction the state transition matrix needs to be computed by solving the differential equation 3.6 utilising as initial condition a identity matrix (I_n).

$$\frac{d}{dt}\mathbf{\Phi}(t, t_0) = A(t)\mathbf{\Phi}(t, t_0) \qquad \text{with } \Phi(t_0, t_0) = I_n \tag{3.6}$$

3.2 Multi-Variable Newton Method

Generally, trajectory design in multi-body dynamical regimes ultimately requires obtaining the solution to a two-point boundary value problem (TPBVP). Different strategies can be applied for the resolution of such problem. In this study a shooting algorithm solved with a multi-variable Newton method. There are many ways to implement a multi-variable shooting scheme, but the one presented is a straightforward extension of the simple root-finding procedure using Newton's method.

The n free variables of the system are collected in a vector $\mathbf{X} = \begin{bmatrix} X_1 \dots X_n \end{bmatrix}$, which, in the multi-body trajectory design, usually includes state vectors, integration times and epochs. A number m of constraints are applied to the free variables and they are collected in a vector $\mathbf{F}(\mathbf{X}) = \begin{bmatrix} F_1(\mathbf{X}) \dots F_m(\mathbf{X}) \end{bmatrix} = 0$. A first time guess vector $\mathbf{X}^0$ is also known, but, in general, it does not satisfy the constraints, therefore: $\mathbf{F}(\mathbf{X}^0) \neq 0$.

The constraint function is first expanded about an the initial guess for the free variable vector as in equation 3.7. Where $D\mathbf{F}(\mathbf{X}^0)$ is a $m \times n$ Jacobian matrix that represents the partial derivatives of the constraints with respect to the free variables and is evaluated at $\mathbf{X}^0$ as in equation 3.8. The system is solved and a new guess solution is found. The process is repeated iteratively till a $\mathbf{X}^*$ solution is found for which $\mathbf{F}(\mathbf{X}^*) \simeq 0$ with a desired tolerance.

$$\mathbf{F}(\mathbf{X}) \approx \mathbf{F}(\mathbf{X}^0) + D\mathbf{F}(\mathbf{X}^0)(\mathbf{X} - \mathbf{X^0}) \tag{3.7}$$

$$D\mathbf{F}(\mathbf{X}^0) = \frac{\partial \mathbf{F}(\mathbf{X}^0)}{\partial \mathbf{X}^0} = \begin{bmatrix} \frac{\partial F_1}{\partial X_1} & \cdots & \frac{\partial F_1}{\partial X_n} \\ \vdots & \ddots & \vdots \\ \frac{\partial F_m}{\partial X_1} & \cdots & \frac{\partial F_m}{\partial X_n} \end{bmatrix} \tag{3.8}$$

Frequently, multi-body trajectory design problems involves a greater number of free variables than constraints, that is $n > m$. Therefore, between all the possible solutions to equation 3.7, the minimum norm solution is usually selected, which is obtained by solving equation 3.9

$$\mathbf{X}^{j+1} = \mathbf{X}^j - D\mathbf{F}(\mathbf{X}^j)^T [D\mathbf{F}(\mathbf{X}^j) \cdot D\mathbf{F}(\mathbf{X}^j)^T]^{-1} \mathbf{F}(\mathbf{X}^j) \tag{3.9}$$

Two different implementations of the multi-variable Newton method will be applied: single shooting and multiple shooting. Both will be described in the following chapters utilising practical examples since their formulation in problem-dependent.

3.3 Differential Equations' Integration

In order to solve the differential equations utilised in the analysis (e.g. equations of motion) the DOP853 algorithm was used, which is an explicit Runge-Kutta method of order 8. Such algorithm is recommended for solving with high precision, as required in this analysis. Further information can be found in the *scipy* documentation [19].

Chapter 4

Transfer in CR3BP

In this chapter the transfer will be computed in the circular restricted three body problem starting from a low Earth circular parking orbit and reaching an halo orbit around L_2 for the Earth-Moon system. The transfer will make use of two manifolds: the exterior of the unstable manifolds around L_2 in the Sun-Earth system and the surface of the stable manifolds around L_2 in the Earth-Moon system. The two manifold will be intersected at a suitable Poincaré section. A reference baseline trajectory is presented in figure 4.1. An alternative solution utilising L_1 Sun-Earth libration point will also be investigated.

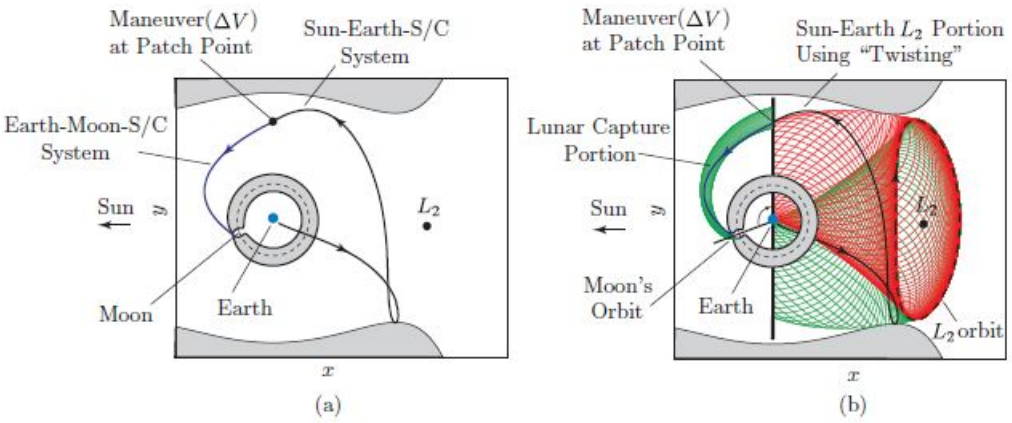

Figure 4.1: Baseline trajectory in Sun-Earth system [13]

4.1 Halo Orbits

Two different halo orbits are required in the analysis. A generic case is here presented, that can be applied from both calculations.

4.1.1 Halo Orbits Computation

Firstly a family halo orbits, from which the desired orbits will be selected, need to be computed starting from the planar Lyapunov orbit. In particular a starting point and a guess period are needed. As a starting point the Lyapunov orbit's $x-z$ plane crossing is selected (where the y coordinate is zero), which will have the following form:

$$\mathbf{p} = (x_0,\ 0,\ 0,\ 0,\ \dot{y_0},\ 0)^T$$

A z displacement (δz_0) is applied, positive for southern halos and negative for northern halos. If the displacement is excessively high, convergence is not reached (in Earth-Moon system a maximum step of 0.1 is admissible, while in the Sun-Earth system the maximum is equal to 0.001). The initial condition will now have the following form:

$$\mathbf{p}_0 = (x_0,\ 0,\ \delta z_0,\ 0,\ \dot{y_0},\ 0)^T$$

A single shooting differential correction method is utilised. As suggested by the name, a single correction in applied to the starting point in order to obtain a desired final condition. Which, for halo orbit computation is another $x-z$ plane crossing, which occurs after half a period. Therefore a state vector, at half period, will have the following structure:

$$\mathbf{p}_{T/2} = (x_d,\ 0,\ z_d,\ 0,\ \dot{y_d},\ 0)^T$$

Due to the selected initial condition the free variables in the problem are the non zero components of the state vector and the period T (i.e. $\mathbf{X} = (x_0,\ z_0,\ \dot{y_0},\ T)$) . While, since the objective is to obtain a state vector as $\mathbf{p}_{T/2}$, the target condition at t_f (where the zero crossing occurs) are $\dot{x_f} = 0$, $\dot{z_f} = 0$ and $y_f = 0$. The target condition can be translated in constraints: $\mathbf{F}(\mathbf{X}) = (\dot{x}_f - \dot{x}_d,\ \dot{z}_f - \dot{z}_d,\ y_f - y_d)^T = (\dot{x}_f,\ \dot{z}_f,\ y_f)^T = 0$. Constraints and free variables in the system are linked by the Jacobian Matrix $D\mathbf{F}(\mathbf{X})$ as in equation 3.7. $D\mathbf{F}(\mathbf{X})$ is composed by the time derivatives of the state vector at t_f and the components of the STM that link free variable and target conditions:

$$D\mathbf{F}(\mathbf{X}) = \begin{bmatrix} \Phi_{41} & \Phi_{43} & \Phi_{45} & \ddot{x}_f \\ \Phi_{61} & \Phi_{63} & \Phi_{65} & \ddot{z}_f \\ \Phi_{21} & \Phi_{23} & \Phi_{25} & \dot{y_f} \end{bmatrix}$$

$D\mathbf{F}(\mathbf{X})$ is not a squared matrix, which implies that the number of free variables is greater than the constraints. In order to solve a squared system, and therefore reducing the computational cost, one free variable is fixed, either x_0 or z_0, eliminating the corresponding column in the $D\mathbf{F}(\mathbf{X})$. In the following the method with z_0 fixed is presented, but an analogue method can be obtained in the other case. The system in equation 4.1 is solved iteratively modifying the initial condition, recomputing the STM and the final state vector until the norm of the variations of the final state is below a desired value.

$$\begin{pmatrix} \delta\dot{x}_f \\ \delta\dot{z}_f \\ \delta y_f \end{pmatrix} = \begin{bmatrix} \Phi_{41} & \Phi_{45} & \dot{x}_f \\ \Phi_{61} & \Phi_{65} & \dot{z}_f \\ \Phi_{21} & \Phi_{25} & y_f \end{bmatrix} \begin{pmatrix} \delta x_0 \\ \delta\dot{y}_0 \\ \delta T \end{pmatrix} \tag{4.1}$$

At each iteration step the equations of motion 2.20 and the differential equations, that yield the STM 3.6, need to be solved with the new initial condition as starting point. It can be shown that the Jacobian matrix in equation 3.6 for the CR3BP, is as in equation 4.2, where $U_{\cdot}$ are the second partial derivatives of the pseudopotential.

$$A = \begin{bmatrix} 0 & 0 & 0 & 1 & 0 & 0 \\ 0 & 0 & 0 & 0 & 1 & 0 \\ 0 & 0 & 0 & 0 & 0 & 1 \\ U_{xx} & U_{xy} & U_{xz} & 0 & 2 & 0 \\ U_{yx} & U_{yy} & U_{yz} & -2 & 0 & 0 \\ U_{zx} & U_{zy} & U_{zz} & 0 & 0 & 0 \end{bmatrix} \tag{4.2}$$

In order to compute a family of halo orbits the process is repeated applying a δz to the starting point ($\mathbf{p}_0$) of the previously computed halo orbit. For a cleared explanation it is advised to check the block diagram in Appendix A.

4.1.2 Monodromy Matrix

After the correct starting point is obtained the monodromy matrix (M) of the halo orbit can be computed. Its eigevalues and eigenvectors contain important information on the halo stability and for the calculation of the associated manifolds. The monodromy matrix is defined as the STM computed over a period as in equation 4.3, where T represents a period.

$$M = \Phi(t_0, t_0 + T) \tag{4.3}$$

For halo orbits the monodromy matrix has two eigenvalues (λ_3, λ_4) equal to one and the remaining four eigenvalues include one real pair (λ_1, λ_2) and one complex pair (λ_5, λ_6). In summary:

$$\lambda_1 > 1, \quad \lambda_2 = \frac{1}{\lambda_1}, \quad \lambda_3 = \lambda_4 = 1, \quad \lambda_5 = \overline{\lambda}_6, \quad |\lambda_5| = 1$$

4.1.3 Halo Orbit Stability

The two pairs of eigenvalues not equal to unity are used to determine the stability of the halo orbits. Stable halo orbits are less subject to perturbations and diverge more slowly from the reference trajectory, therefore requiring less propellant for station-keeping. Two stability indices can be defined from the two pairs of eigenvalues as in equation 4.4 [20]. If the are both less than 1 the orbit is stable.

$$\nu_i = \frac{1}{2}\left(\lambda_i + \frac{1}{\lambda_i}\right) \qquad i = 1/2{,}5/6 \tag{4.4}$$

A halo with stability index close to unity should be selected as destination orbit in order to reduce the station-keeping costs and extended the mission life.
In figure 4.2 a family of northern halo orbits in presented which the stable ones are in green. While in figure 4.3 the selected halo for the analysis in presented.

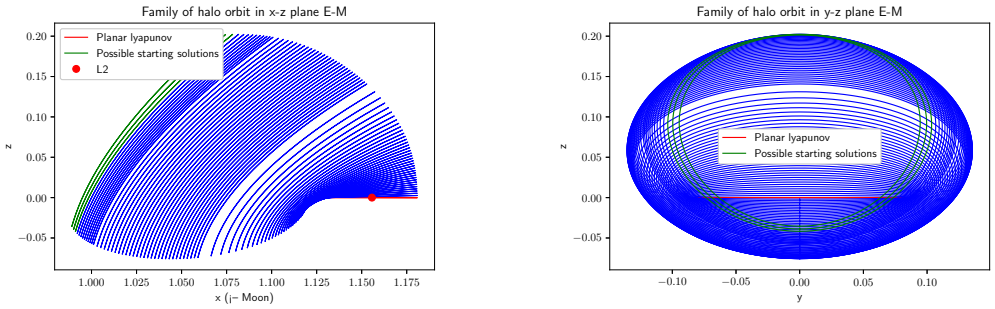

(a) Northern Moon L_2 Halo Family $x-z$ view **(b)** Northern Moon L_2 Halo Family $y-z$ view

Figure 4.2: Northern Moon L_2 Halo Family

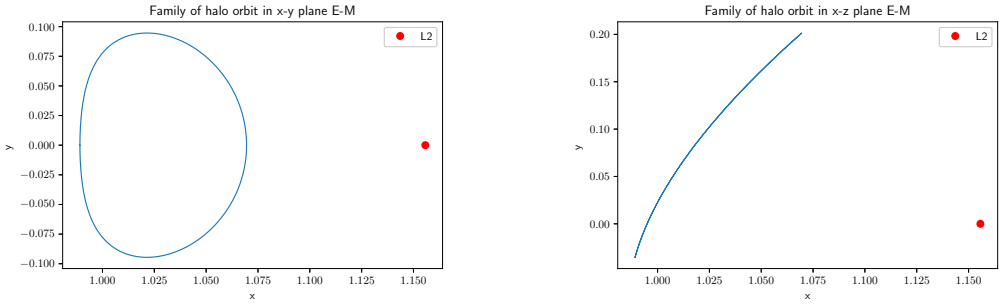

(a) Selected Moon L_2 Halo $x-y$ view **(b)** Selected Moon L_2 Halo $x-z$ view

Figure 4.3: Selected Moon L_2 Halo

4.2 Manifolds

Stable and unstable manifolds can be computed from a reference halo orbits and are associated with real eigenvalues of the monodromy matrix. The eigenvector associated to the real eigenvalue greater than 1 is used to obtain the unstable manifold, while the eigenvector associated to the real eigenvalue less than 1 the stable one. The procedure will be described for the construction of a stable manifold, but a similar procedure can be implemented for the computation of the unstable one by simply changing the eigenvector utilised.

The starting point for the integration is obtained applying a displacement to the state vector at the halo at t_0 as in equation 4.5, where $Y^s(\mathbf{p_0})$ is the normalized eigenvector associated with the stable eigenvalue (with module less then unitary). Suitable values of ε correspond to position displacements of 200 km ($1.3 \cdot 10^{-4}$ dimensionless) in the Sun-Earth system and 50 km ($1.3 \cdot 10^{-4}$ dimensionless) in the Earth-Moon system. Plus and minus sign correspond to the due branches (from outside to halo and from secondary body to halo). The correspondence is not univocal, but depends on the orbit dimension.

$$\mathbf{p}^s(\mathbf{p_0}) = \mathbf{p_0} \pm \varepsilon Y^s(\mathbf{p_0}) \tag{4.5}$$

For the manifold associated with a halo point at $t \neq t_0$ one can simply use the state transition matrix to transport the eigenvectors from t_0 to t as in equation 4.6. An example of manifolds in the Earth-Moon system is presented in figure 4.4.

$$Y^s(\mathbf{p}(t)) = \Phi(t, t_0) Y^s(\mathbf{p_0}) \tag{4.6}$$

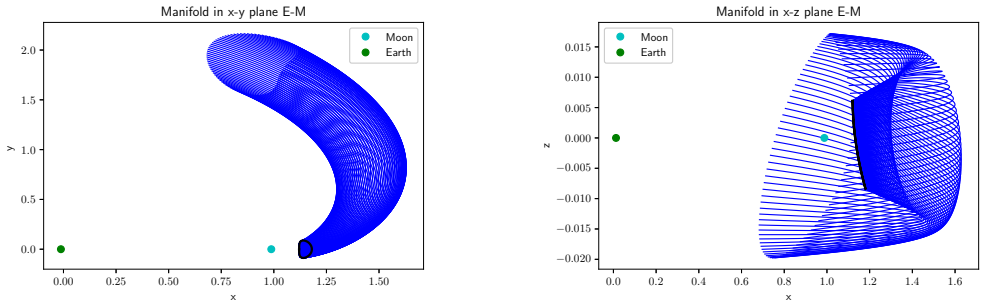

(a) Stable Earth-Moon L_2 Manifold $x-y$ view **(b)** Stable Earth-Moon L_2 Manifold $x-z$ view

Figure 4.4: Stable Earth-Moon L_2 Manifold

4.3 Manifolds intersection

The stable manifold in the Earth-Moon system (in green in figure 4.1) and the unstable manifold in the Sun-Earth system (in red in figure 4.1) intersect at a Poincaré section, which is chosen coinciding with the Earth's x coordinate for simplicity.

4.3.1 Coordinate transformation

In order to find an intersection between the manifolds they both need to be written in Sun-Earth coordinates. Therefore a coordinate transformation for the Earth-Moon manifold is required. In the transformation the moon inclination is considered negligible.

The time transformation in given by equation 4.7, where ω_S and ω_m are the angular velocity of the two systems and $\bar{t}$ represents the quantity in the Sun-Earth system.

$$\bar{t} = \frac{\omega_S}{\omega_M} t \tag{4.7}$$

The transformation of position is represented in equation 4.8. $C(t)$ is the rotation matrix as in equation 4.9, a_M the average distance between Earth and Moon, a_S the distance between the Sun and the center of gravity of the Earth-Moon system, θ_M represent the angle between the x and $\overline{x}$ axis as in equation 4.10 and θ_{M0} is the starting angle between the axis and coincides with the phase at arrival in the analysed trajectory. A schematic representation of the system in analysis, defined ad bicircular model, can be found in figure 4.5

$$\begin{pmatrix} \overline{x} \\ \overline{y} \\ \overline{z} \end{pmatrix} = \begin{pmatrix} 1-\mu_S \\ 0 \\ 0 \end{pmatrix} + \frac{a_M}{a_S} C(t) \begin{pmatrix} x \\ y \\ z \end{pmatrix} \tag{4.8}$$

$$C(t) = \begin{bmatrix} \cos(\theta_M) & -\sin(\theta_M) & 0 \\ \sin(\theta_M) & \cos(\theta_M) & 0 \\ 0 & 0 & 1 \end{bmatrix} \tag{4.9}$$

$$\theta_M = \left(1 - \frac{\omega_M}{\omega_M}\right) t + \theta_{M0} \tag{4.10}$$

Ones the two halo orbits and the respective manifolds are selected the free variable of the system is the phase (θ_{M0}) at Moon arrival. Usually a vast range of phases produce a suitable solution with similar results in terms of ΔV, but slightly different transfer times.

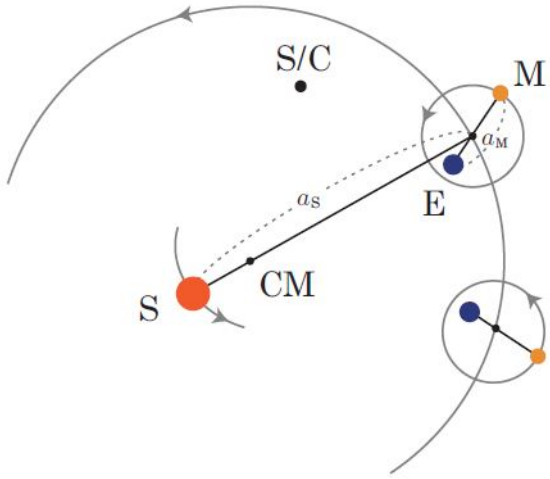

Figure 4.5: Bicircular Model

4.3.2 2D intersection

In the 2D intersection the z coordinate is neglected, therefore intersection between manifolds can be researched in the $y - v_y$ plane, with the goal of minimizing ΔV required. An example of manifolds intersection in $y - v_y$ plane at Poincaré Section is presented in figure 4.6.

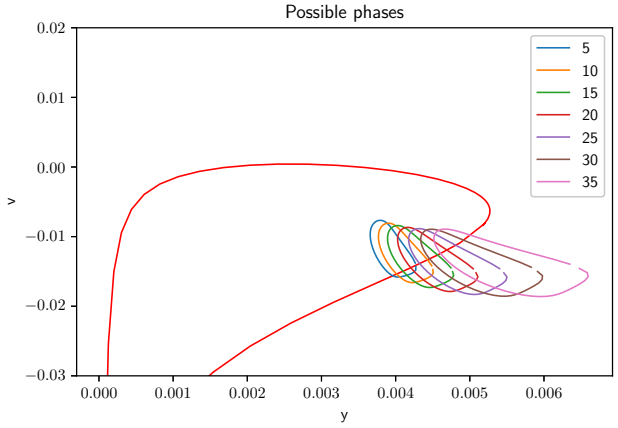

Figure 4.6: Intersection Manifolds in $y - v_y$ plane

However the z coordinate can not always be neglected and therefore in the majority of cases a 3D intersection in required.

4.3.3 3D intersection

In 3D intersection the goal is to guarantee the position continuity of the trajectory rather then minimizing the ΔV required. Therefore the intersection is found in the $y-z$ plane at the Poincaré section and normally two solutions are possible. If a stable halo orbit is selected the Moon phase does not influence significantly the manifolds intersection. An example of manifolds intersection in $y-z$ plane at Poincaré Section is presented in figure 4.7.

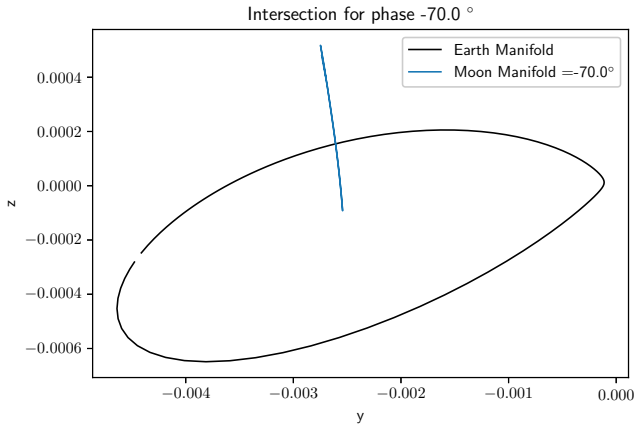

Figure 4.7: Intersection Manifolds in $y-z$ plane

4.4 Targeting LEO

In order to obtain a trajectory departing from a low Earth circular orbit the exterior of the unstable manifold is utilized. Therefore the velocity at Poincaré section is slightly modified and the trajectory is integrated backward iteratively till a solution reaching the desired LEO orbit is obtained. The function *fmin* in the *scipy.optimize* package for *Python* is used in order to complete the local optimization. Such function utilise a Nelder-Mead simplex algorithm [21] to find the minimum of function of one or more variables. In this case all three velocity components at Poincaré section are allowed to vary.

The final trajectory requires one correction in velocity at Poincaré section ΔV_2 and in order to obtain a total transfer cost also the ΔV_1 for LEO departure can be calculated.

4.5 $L_1 - L_2$ and $L_2 - L_2$ trajectories

Shane Ross et al [13] solution utilises the exterior of the L_2 manifold in the Sun-Earth system to reach the Poincaré section and the intersection found in the positive y direction. Such solution will be referred in the future as $L_2 - L_2$ solution. As underlined by Han-qing Zhang and Yan-jun Li [22] it is also possible to obtain a weak stability transfer utilising the exterior of the L_1 manifold in the Sun-Earth system, referred in the future as $L_1 - L_2$ solution. In this case intersection at Poincaré section in found for negative y values. An example of such transfer is shown in figure 4.8.

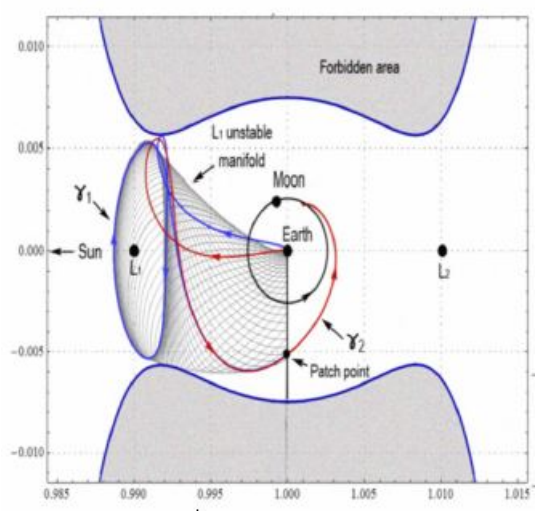

Figure 4.8: Example of $L_1 - L_2$ trajectory

Han-qing Zhang and Yan-jun Li [22] suggest that utilising $L_1 - L_2$ transfer can reduce travel time and costs compared to the $L_2 - L_2$ solution. Both solutions will be investigated in this analysis and results will be confronted in order to verify such claim.

4.6 Examples of Baseline Trajectories

Two examples of computed $L_1 - L_2$ and $L_2 - L_2$ trajectories are presented in figure 4.9.

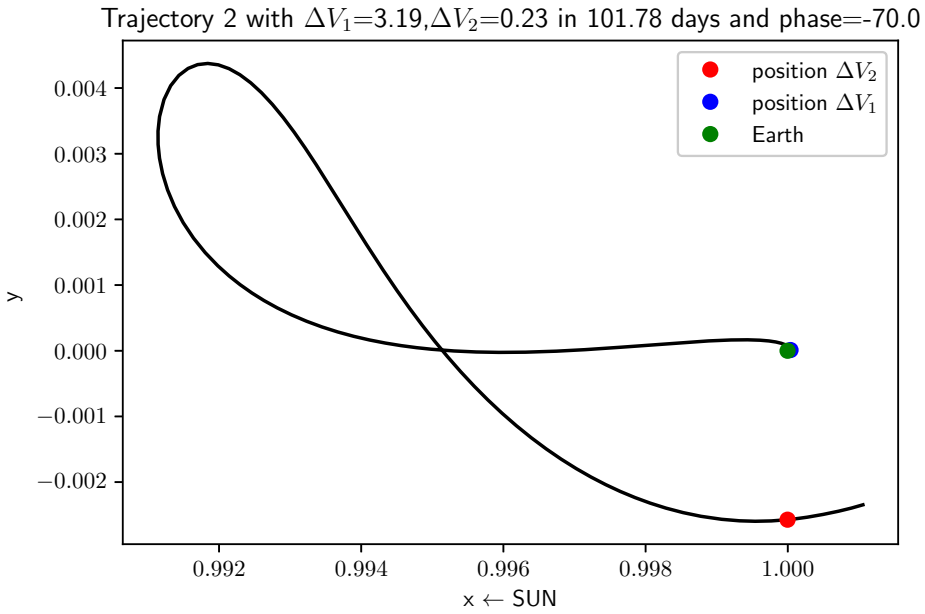

(a) $L_1 - L_2$ trajectory

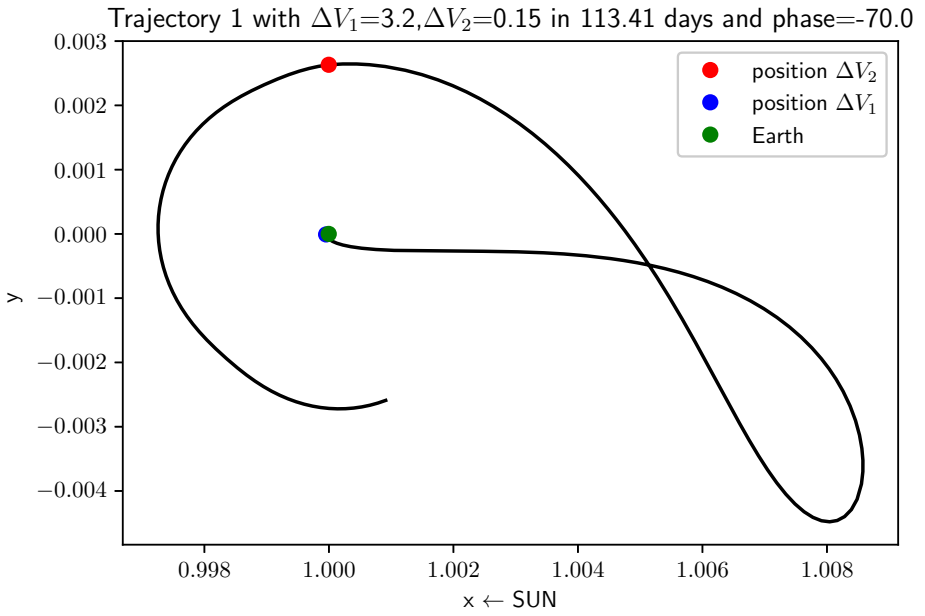

(b) $L_2 - L_2$ trajectory

Figure 4.9: Examples of $L_1 - L_2$ and $L_2 - L_2$ trajectories

Chapter 5

Transfer in Perturbed J2000

In this chapter the limits of the CR3BP are underlined and a more realistic model is introduced. In such model planetary ephemerides are included and they are obtained utilising a python implementation for SPICE toolkit, which will be briefly described. Finally the trajectory correction implemented to compute a perturbed solution is illustrated.

5.1 Limits to the CR3BP

The CR3BP model predicts the motion of a body of negligible mass under the influence of the gravitation field produced by primary and secondary bodies that orbit in a circular path around the center of gravity of the three mass system. The motion in the system is considered planar. Such model produces a preliminary approximation of the reality, but a good number to hypothesis are made and phenomena are neglected, that could have a significant impact on the solution. In particular:

- Planetary trajectories are not planar and orbits have eccentricities not equal to zero. In particular Earth eccentricity is equal to 0.0167, while the Moon eccentricity is 0.0549. Furthermore the inclination of the Moon, with respect to the ecliptic, in variable throughout the year, ranging from a minimum of $4°59'$ to a maximum of $5°18'$ in the positive or negative direction depending on the position of the line of nodes with respect to the reference system. An many other phenomena occur that create divergences from the CR3BP

- Each celestial and artificial body's motion is influenced by every other body in the system. A notable example of this phenomena if the fact that the existence of Neptune was hypothesised before its actual discover, due to the

perturbation it produced on the orbit of Uranus, which could not be explained otherwise.

- Other perturbing phenomena are present, such as solar pressure, due to photons pressing on celestial and artificial bodies. Generally, a part from satellites in which the ratio volume mass is high, this phenomena can be neglected. The acceleration produced on a body is reported in equation 5.1, where p is the solar pressure, which decreases as distance from the Sun increases (in proximity of Earth is equal to 4.5 10^{-6} N/m^2).

$$a_{sr} = p\frac{S}{m} \tag{5.1}$$

Therefore an analysis relaxing some constraints was conducted and the results compared with the baseline solution.

5.2 Applied Model

In the analysis conducted only some of the previously introduced effects are considered, but further components can be easily added in the future. In particular:

- Solar pressure was not considered due to the low contribute compared to the complexity introduced in the STM matrix calculation needed for trajectory correction.
- Bodies included in the analysis are: Sun, Earth and Moon. No additional body was included since their effect is expected to be negligible and would add additional term in the equation of motion with the risk of higher computational cost.

For the considered bodies the actual position in space in required, since the removal of the hypothesis of circular planar orbit. Position are provided by ephemerides, which are tables that provide trajectory of naturally occurring astronomical objects as well as artificial satellites in terms of position and velocity over time [23]. Analysis that include ephemerides are inevitably dimensional, therefore all quantities and equations introduced from this moment onward will be dimensional, with time in seconds part the J2000 epoch and distance in kilometers.

5.2.1 Equation of motion

The equation of motion are obtained from the N-body problem force equation 2.3 and are reported, in vector notation, in equation 5.2.

$$\mathbf{a} = -\frac{Gm_{\odot}}{r_{\odot i}^3}\mathbf{r}_{\odot\mathbf{i}} - \frac{Gm_{\oplus}}{r_{\oplus i}^3}\mathbf{r}_{\oplus\mathbf{i}} - \frac{Gm_{\leftmoon}}{r_{\leftmoon i}^3}\mathbf{r}_{\leftmoon\mathbf{i}} \tag{5.2}$$

The position of correct bodies is needed and can be obtained from planetary and lunar ephemerides utilising the SPICE toolkit.

5.3 SPICE Toolkit

SPICE is an observation geometry information system, provided by NAIF (Navigation and Ancillary Information Facility), acting under the directions of NASA's Planetary Science Division, to assist scientists and engineers in planning and interpreting scientific observations from space-based instruments and planetary exploration missions. Nowadays it is regularly used in mission design, mission operations, and observation planning [24].

The SPICE project start in 1982 in responds to a report detailing problems with and providing recommendations for the archival treatment of data returned from NASA's Space Science Missions. The first efforts where made during the Voyager mission, but the first real use of SPICE technology occurred on the Magellan mission to Venus; here the Navigation Team produced spacecraft orbit data in the SPICE SPK format that is still in use today.

Important data set in SPICE, such as navigation and other ancillary information providing precision observation geometry, are included in kernels. Different types of kernels exist, but in this analysis the mainly used one is the SPK kernel, containing space vehicle or target body trajectory (i.e. ephemerides).

Different reference frames can be utilised in SPICE, both defined by users and already implemented, but calculations are computed in J2000 and if required translated in other reference frames. Therefore, in order to reduce computational cost, in it convenient to work in J2000.

5.3.1 J2000 Reference System

The definition of the J2000 reference frame is based on the Earth's equatorial plane and on the Ecliptic plane, determined from observations of planetary data. The X-direction is given by the intersection of equatorial and ecliptic planes, called vernal equinox. The Z-direction is normal to the mean equator of date at epoch J2000 TDB, which is approximately Earth's spin axis orientation at that epoch. The Y-direction complete the set of three. A schematic representation can be found in figure 5.1.

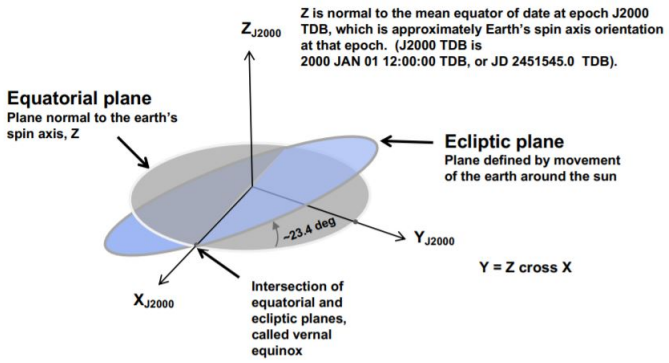

Figure 5.1: J200 reference system [24]

5.3.2 Three body Problems Reference Frames

Reference frames such as the one used in the CR3BP are not present in the SPICE toolkit, but can be easily added as a Two-Vector Frame. Further information can be found in SPICE Toolkit Documentation [25].

5.3.3 Used functions

The functions SPICE functions utilised in the analysis are:

- **bodvrd**: supplies physical data, radius and gravitational parameter values, of celestial bodies;
- **spkezr**: return the state vector, position and velocity, of a target body relative either to an observing body or a specific point, at a specific time for a defined reference system.
- **sxform**: returns state transformation matrix between two defined reference frames;
- **str2et**: return second past J2000 epoch from a date in a string;
- **et2utc**: opposite to **str2et**

5.4 Baseline Trajectory

The CR3BP trajectory needs to be transformed in dimensional quantities and rotated to J2000 reference system in order to obtain the baseline trajectory. An example of baseline trajectory is represented in figure 5.2.

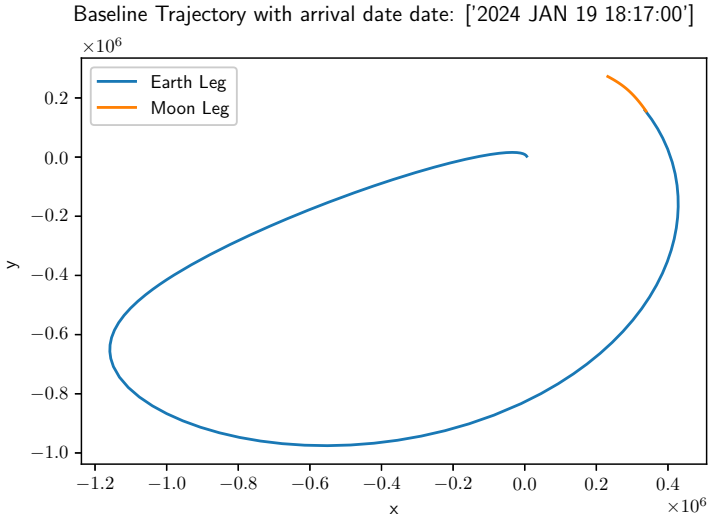

Figure 5.2: Baseline trajectory

5.5 Trajectory Correction

By simply integrating the starting point of the baseline trajectory in the perturbed equations of motion a deeply different trajectory is found. Therefore slight correction to the reference trajectory need to be computed in order to obtain convergence in the ephemerides model. Such correction are computed utilising the multiple shooting method.

5.5.1 Multiple Shooting Differential Correction

Multiple shooting method can be considered an extension of the single shooting method presented in 4.1.1, where more than 2 nodes are included in the analysis.

The first step is the nodes' definition. Since a DOP853 method was utilised for integration, without constraints on time evaluation, the number of points utilised in the baseline trajectory definition is limited (less then 200 for each segment) and more dense in critical part of the trajectory. Therefore they can be utilised as nodes for the multiple shooting differential correction since they provide a good compromise between accuracy and computational cost requirements. In the analysis conducted the following constraints are imposed:

- Nodes can vary in position between baseline and perturbed trajectory, but not in time. Therefore corresponding nodes in the two trajectories occur at

the same time and the transfer time between two consecutive nodes does not vary between baseline and perturbed trajectory.

- Perturbed trajectory is continuous in position always and in velocity expect for one point, where the ΔV_2 occurs in the baseline trajectories. Therefore no more correction are introduced compared to the CR3BP.
- The two legs of the trajectory are treated separately with additional constraints imposed at beginning and end. The trajectory from Earth to Poincaré section will be refereed as Earth leg and the trajectory from Poincaré section to Moon as Moon leg.

With this consideration in mind free variables and constraint vector for the multi-variable Newton method can be defined. For both legs the free variables' vectors $\mathbf{X}$ are $6N$ vectors composed by the state vector at each node (with N number of nodes), as in equation 5.3.

$$\mathbf{X} = [\mathbf{x_1}\ \mathbf{x_2}\ ...\mathbf{x_i}\ ..\mathbf{x_n}]^T \quad \text{with} \quad \mathbf{x_i} = [x_i\ y_i\ z_i\ u_i\ v_i\ w_i]^T \tag{5.3}$$

While $\mathbf{F}(\mathbf{X})$ constraints vector is comprised by:

- A core vector of dimensions $6(N-1)$ including constraints of internal continuity in position and velocity as in equation 5.4. Where the primed components are the solutions of integration of the perturbed equation of motion 5.2 (e.g. $\mathbf{x'_3}$ is the state vector resulting from integration of 5.2 from time t_2 to t_3 with $\mathbf{x'_2}$ as starting point);
- Up to 6 additional elements can be included as additional constraints, usually at the start or end of the trajectory.

$$\mathbf{F}\begin{pmatrix} \mathbf{x_1} \\ \mathbf{x_2} \\ \vdots \\ \mathbf{x_i} \\ \vdots \\ \mathbf{x_{N-1}} \end{pmatrix} = \begin{pmatrix} \mathbf{x'_2} \\ \mathbf{x'_3} \\ \vdots \\ \mathbf{x'_i} \\ \vdots \\ \mathbf{x'_{N-1}} \end{pmatrix} - \begin{pmatrix} \mathbf{x_2} \\ \mathbf{x_3} \\ \vdots \\ \mathbf{x_{i+1}} \\ \vdots \\ \mathbf{x_N} \end{pmatrix} \tag{5.4}$$

The Jacobian matrix $D\mathbf{F}(\mathbf{X})$ is defined as in equation 3.8 (where I is an identity matrix). For the core components of the constrain vector the corresponding elements of the $D\mathbf{F}(\mathbf{X})$ are as in equation 5.5. While components due to additional constraints may vary depending on the constraint imposed.

$$D\mathbf{F}(\mathbf{X}) = \begin{bmatrix} \phi(t_2, \mathbf{x_1}) & -I & 0 & 0 & 0 & \cdots & 0 \\ 0 & \phi(t_3, \mathbf{x_2}) & -I & 0 & 0 & \cdots & 0 \\ \vdots & & & \ddots & & & \vdots \\ 0 & \cdots & 0 & 0 & 0 & \phi(t_N, \mathbf{x_{N-1}}) & -I \end{bmatrix} \tag{5.5}$$

5.5.2 Moon Leg

The moon leg is the first leg to be corrected. As additional constraint, the position at Halo arrival (i.e. at end) is required to be equal to the baseline trajectory one. Consequently $D\mathbf{F}(\mathbf{X})$ is a non square $[6(N-1)+3 \text{ X } 6N]$ matrix and therefore the minimum norm solution needs to be calculated as in equation 3.9. Convergence usually occurs in a limited number of iterations. An exaple of comparison between baseline and perturbed trajectory is presented in figure 5.3.

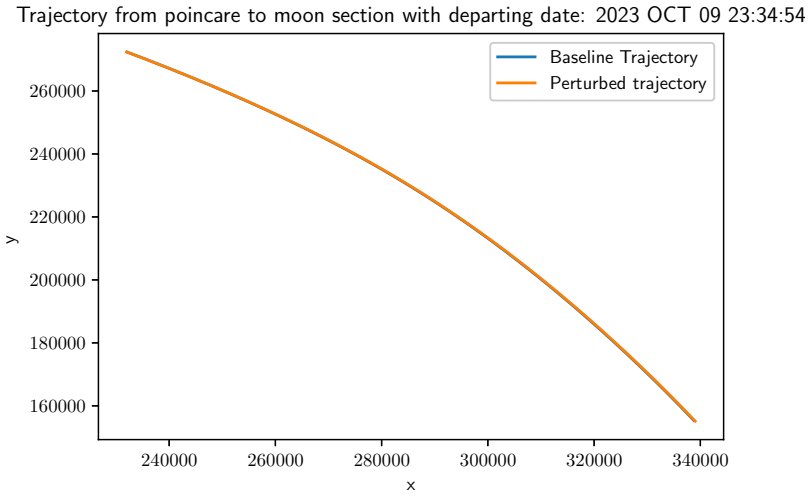

Figure 5.3: Comparison baseline and perturbed trajectory for Moon leg

5.5.3 Earth Leg

For the second part convergence is more complex to achieve and multiple steps are required increasing computational time. Firstly a multiple shooting procedure is implemented with additional constraints at end position (i.e. at Poincare section), forcing it to be coincident to the start position of the perturbed Moon trajectory. Convergence is fast, but the starting point of the perturbed Earth leg is usually far from the desired one. Therefore additional corrections are required. This first solution is then utilised as baseline trajectory for a second multiple shooting algorithm where constraints are: on end position as before and on the radius at start position, which is required to be equal to desired LEO altitude. This second requirement is usually not met, but a lower starting orbit in reached. Consequently a third step is required. In this case a procedure analogue to the one used in the CR3BP to target the LEO orbit (see section 4.4) is implemented, with starting vector coinciding with the previously achieved state vector at Poincaré section.

This procedure allows for good convergence also for the Earth leg, but usually modifies the transfer time compared to the CR3BP. An example of the convergence process, including the different stages, is reported in figure 5.4.

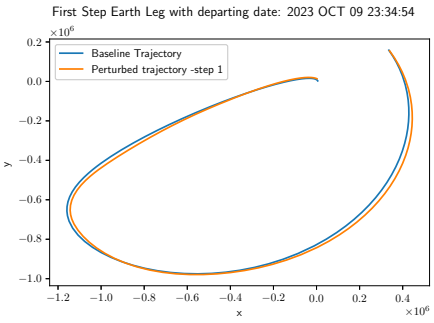

(a) First step. Achieved radius = 17236 km

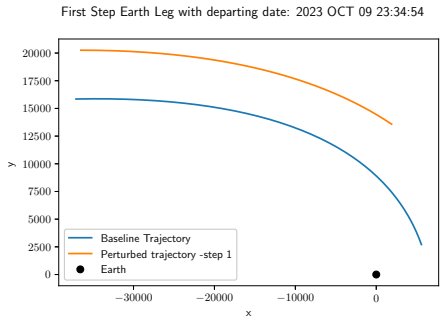

(b) First step. Zoom near Earth

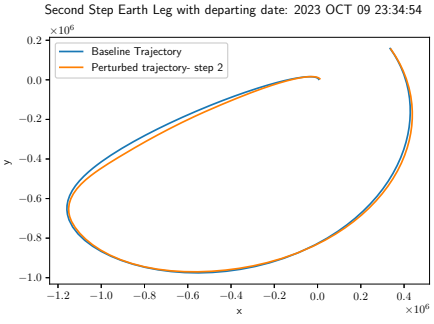

(c) Second step. Achieved radius = 12721 km

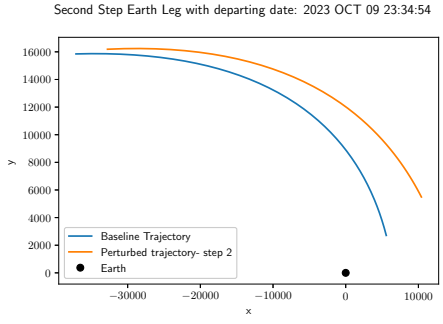

(d) Second step. Zoom near Earth

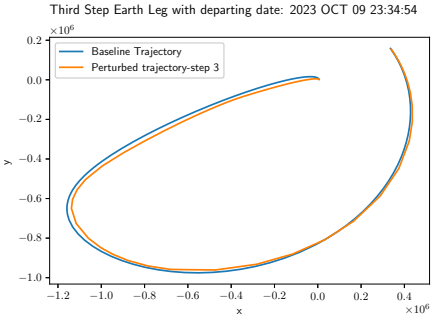

(e) Third step. Achieved radius = 6571 km

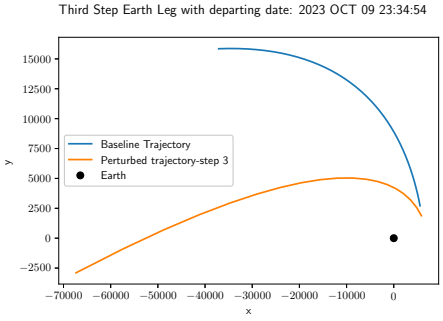

(f) Third step. Zoom near Earth

Figure 5.4: Earth Leg Correction Steps

5.5.4 Example of Perturbed Trajectory

An example of perturbed trajectory, after correction, with used the baseline trajectory in figure 5.2 is represented in figure 5.5

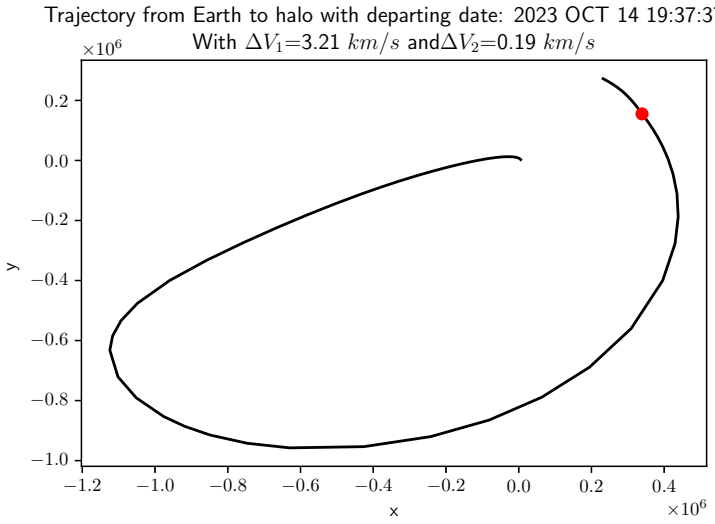

Figure 5.5: Perturbed trajectory

Chapter 6

Results and Conclusions

In this chapter results are presented, final conclusion are drawn and future development possibilities are underlined. A comparison between trajectories that utilise L_1 and L_2 Sun-Earth libration points will be conducted as well as a comparison between the solutions obtained in the CR3BP and the ephemerides model.

6.1 Effect of Moon Phase

Since the objective of the transfer is insertion in a halo orbit, orbit stability is an essential parameter in order to limit station-keeping costs. Therefore a limited range of halo orbits can be selected, those with stability index close to one. For such orbits the Moon phase impacts transfer time but does not produce significant variation in transfer cost. Such behaviour can be linked to the different manifold configuration: fixing time of integration, for a stable halo the manifold is confined near the halo orbit and its section does not increase excessively, while a manifold, departing from less stable orbits, reaches greater distances and its section dimensions increases with distance. An example of comparison is show in figure 6.1

For each phase, two intersections are possible, but usually one has a lower cost compared to the other, due to the higher ΔV at Poincare Section (refereed as ΔV_2).

Example of trajectories with different arrival phases are presented in figure 6.2 and the transfer costs and times are summarised in table 6.1 for a $L_2 - L_2$ transfer in the CR3BP.

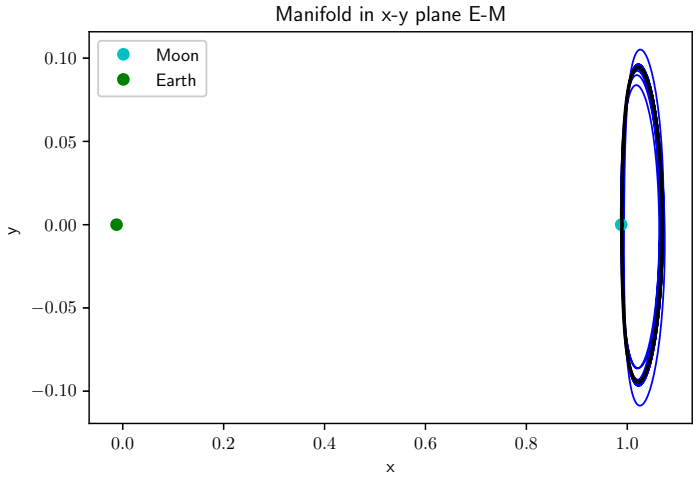

(a) Stable manifolds of a stable halo

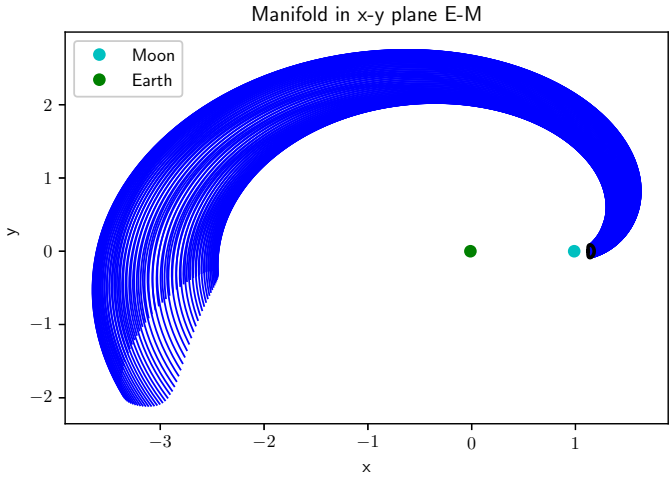

(b) Stable manifolds of an unstable halo

Figure 6.1: Comparison between Manifolds of stable and unstable Halo

6.2 Comparison Between $L_2 - L_2$ and $L_1 - L_2$ Transfers in CR3BP

As previously explained, in order to reach an halo orbit around L_2 in Earth-Moon system, both the L_1 and L_2 unstable Earth manifolds can be utilised. Both options produce viable transfers with comparable costs (marginally higher for $L_1 - L_2$ option in the CR3BP), but the $L_1 - L_2$ solutions have lower transfer time by 10 days.

Example of $L_2 - L_2$ trajectories are presented in figure 6.2 and the transfer costs and times are summarised in table 6.1, while example of $L_1 - L_2$ trajectories are presented in figure 6.3 and the transfer costs and times are summarised in table 6.2.

Solution	Phase	ΔV_1 km/s	ΔV_2 km/s	ΔV_{tot} km/s	$Time$ [days]
1	-70°	3.195	0.150	3.345	113.411
2	-70°	3.191	0.637	3.828	115.956
1	-80°	3.191	0.149	3.340	114.725
2	-80°	3.195	0.633	3.828	120.899
1	-100°	3.191	0.149	3.340	112.354
2	-100°	3.192	0.633	3.825	114.833
1	-110°	3.195	0.147	3.342	116.409
2	-110°	nc*	nc	nc	nc
1	-120°	3.197	0.147	3.344	115.602
2	-120°	nc	nc	nc	nc

Table 6.1: Cost And Transfer Times for different phases transfer $L_2 - L_2$
*nc=not possible to reach desired LEO altitude

Solution	Phase	ΔV_1 km/s	ΔV_2 km/s	ΔV_{tot} km/s	$Time$ [days]
1	-30°	3.192	0.626	3.818	100.305
2	-30°	3.191	0.238	3.429	105.372
1	-40°	3.194	0.532	3.726	106.114
2	-40°	3.191	0.191	3.382	103.122
1	-50°	nc*	nc	nc	nc
2	-50°	3.193	0.265	3.458	106.040
1	-70°	nc	nc	nc	nc
2	-70°	3.193	0.231	3.424	101.779

Table 6.2: Cost And Transfer Times for different phases transfer $L_1 - L_2$
*nc=not possible to reach desired LEO altitude

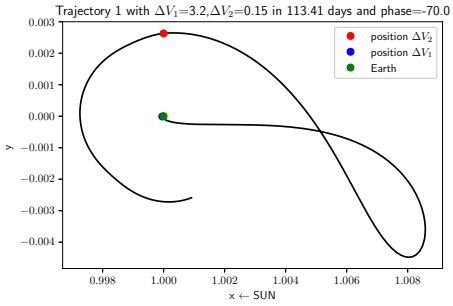

(a) Phase $-70°$, Solution 1

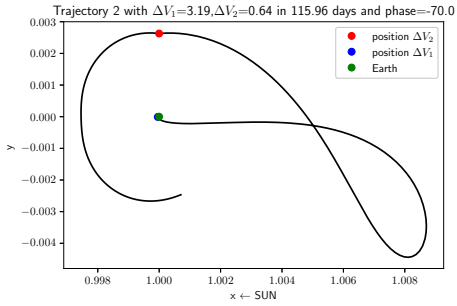

(b) Phase $-70°$, Solution 2

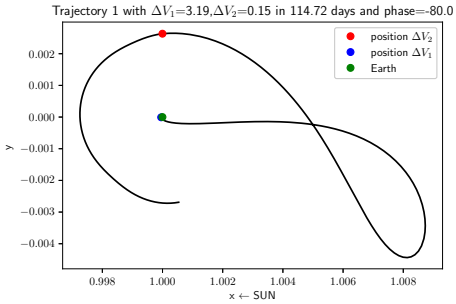

(c) Phase $-80°$, Solution 1

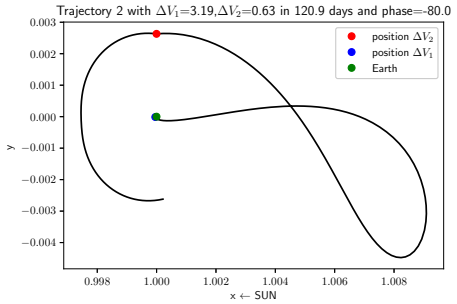

(d) Phase $-80°$, Solution 2

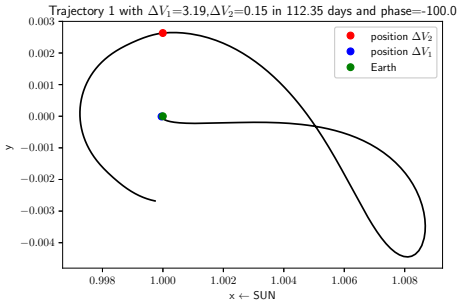

(e) Phase $-100°$, Solution 1

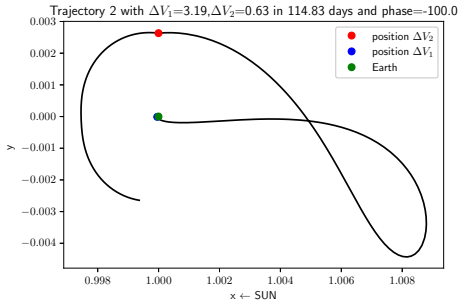

(f) Phase $-100°$, Solution 2

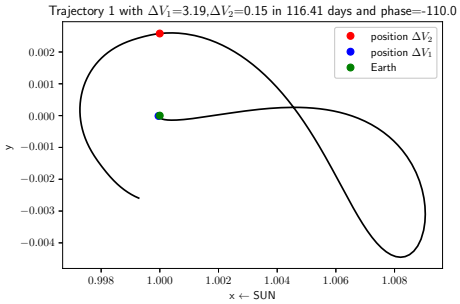

(g) Phase $-110°$, Solution 1

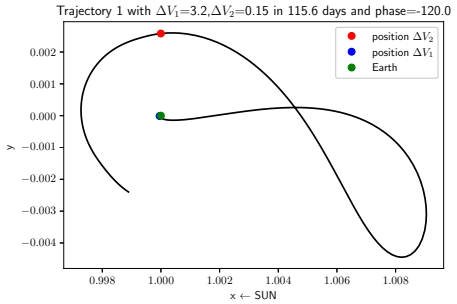

(h) Phase $-120°$, Solution 1

Figure 6.2: Transfer $L_2 - L_2$ comparison between phases

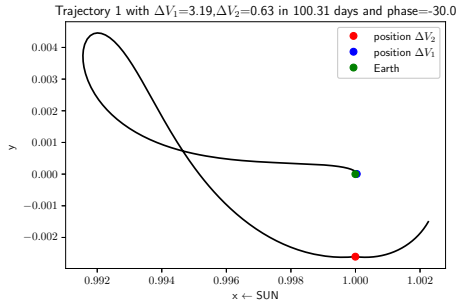

(a) Phase $-30°$, Solution 1

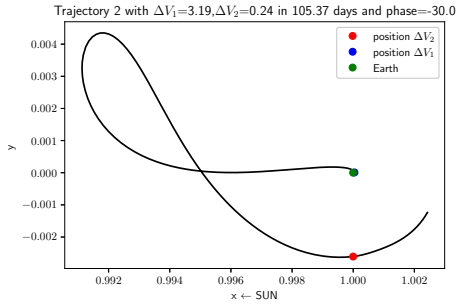

(b) Phase $-30°$, Solution 2

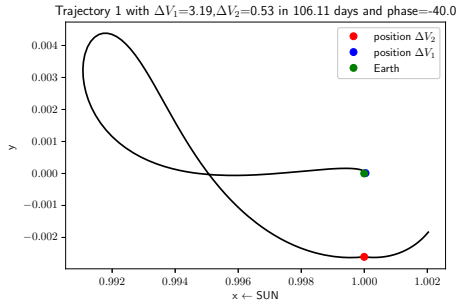

(c) Phase $-40°$, Solution 1

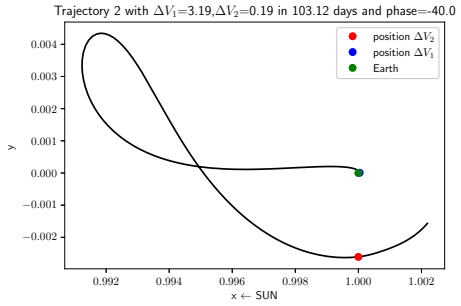

(d) Phase $-40°$, Solution 2

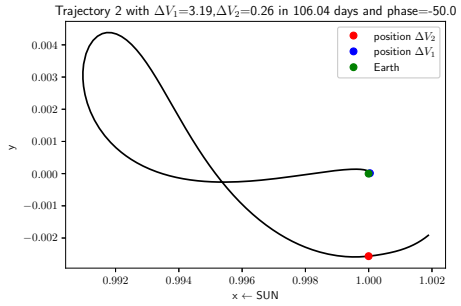

(e) Phase $-50°$, Solution 2

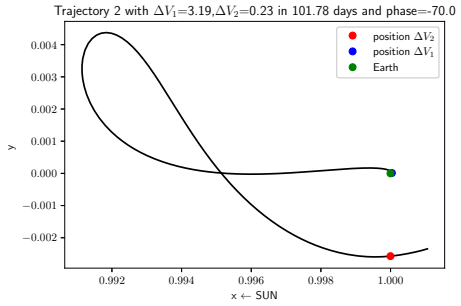

(f) Phase $-70°$, Solution 2

Figure 6.3: Transfer $L_1 - L_2$ comparison between phases

6.3 Effects of Perturbations

The introduction of planetary and lunar ephemerides produces a deviation from the ideal solution obtained in the CR3BP, but the two trajectories are not that dissimilar graphically (in figure 6.4 a comparison between baseline trajectory, obtained with the CR3BP, and the perturbed trajectory in the ephemerides correct inertial Earth Moon system is presented).

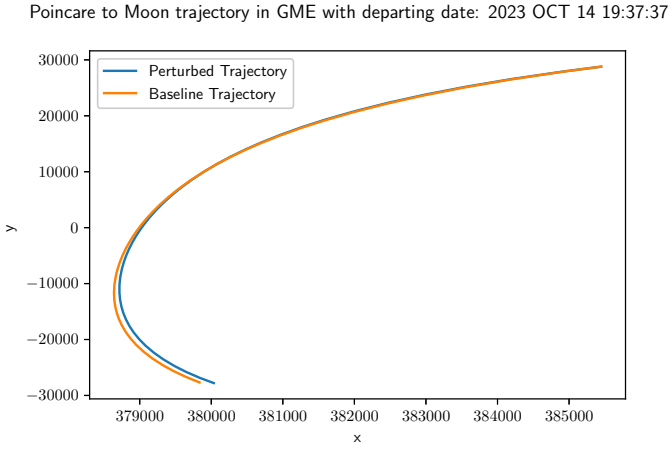

Figure 6.4: Comparison between baseline trajectory and the perturbed trajectory in the GEM

This is especially true for the transfer from Poincaré section to Moon Halo, therefore no high cost maneuver is required for halo insertion. However a slight variation in the transfer cost and time occurs. Part of transfer cost variation can be traced back to the correction due to Moon's inclination (not considered in the CR3BP). Furthermore the variation of the perturbing bodies position throughout the year causes differences in the transfer cost depending on the starting date. While flexibility in departure time from LEO is an essential requirement for convergence with the maximum admissible variation set by the user, producing solutions with a difference is of at least a couple of hours from the baseline.

Example of $L_2 - L_2$ and $L_1 - L_2$ trajectories are presented respectively in figure 6.5, 6.6 and 6.7, 6.8 , while the transfer costs and times are summarised respectively in table 6.3 and 6.4, utilising data considering possible arrival dates in 2024 and a phase of $-70°$ for both trajectory.

Similar results can be found for both $L_2 - L_2$ and $L_1 - L_2$ trajectories, but in the $L_2 - L_2$ the difference in ΔV between the CR3BP and the perturbed trajectory is greater. In the $L_1 - L_2$ trajectories the ΔV_{tot} is within a 200 m/s of difference from the CR3BP results and in some cases also the mission costs decreases with the introduction of perturbation as well as travel time, dropping below 100 day at times. While in the $L_2 - L_2$ the difference between the CR3BP trajectory and the perturbed one can reach up to 300 m/s and, with one exception for the considered case, while travel time increases of up to 21 days. However travel time and cost can be slightly influenced by the flexibility allowed in the LEO orbit altitude.

Moon Arrival	r_{LEO} km	ΔV_1 km/s	ΔV_2 km/s	ΔV_{tot} km/s	$Time$ [days]	Δt [hours]
CR3BP	6571.051	3.195	0.150	3.345	113.4119	0
19/01/24	6571.049	3.210	0.300	3.510	113.816	9.710
18/02/24	6571.105	3.190	0.4006	3.590	114.178	18.407
18/03/24	6571.123	3.210	0.390	3.600	113.584	4.133
17/04/24	6570.971	3.200	0.240	3.440	114.373	23.079
17/05/24	6570.774	3.240	0.210	3.450	120.752	176.183
16/06/24	6571.196	3.190	0.220	3.410	122.833	226.113
15/07/24	6570.978	3.200	0.260	3.460	113.447	0.847
14/08/24	6570.911	3.190	0.330	3.520	113.168	-5.833
12/09/24	6571.001	3.210	0.360	3.570	115.330	46.048
12/10/24	6571.033	3.220	0.410	3.630	114.908	35.928
10/11/24	6571.021	3.200	0.350	3.550	114.752	32.164
10/12/24	6571.057	3.220	0.330	3.550	114.474	25.5070

Table 6.3: Cost And Transfer Times for different launch dates transfer $L_2 - L_2$

Moon Arrival	r_{LEO} km	ΔV_1 km/s	ΔV_2 km/s	ΔV_{tot} km/s	$Time$ [days]	Δt [hours]
CR3BP	6570.929	3.193	0.231	3.424	101.779	0
19/01/24	6570.998	3.210	0.190	3.400	96.944	-116.045
18/02/24	6570.952	3.200	0.220	3.420	98.475	-79.306
18/03/24	6570.531	3.190	0.220	3.410	98.349	-82.322
17/04/24	6570.627	3.190	0.230	3.420	97.811	-95.241
17/05/24	6571.092	3.200	0.280	3.480	96.778	-120.027
16/06/24	6571.079	3.200	0.330	3.530	105.160	81.149
15/07/24	6571.044	3.220	0.360	3.580	102.016	5.680
14/08/24	6570.542	3.240	0.360	3.600	104.518	65.739
12/09/24	6571.565	3.200	0.320	3.520	110.947	220.024
12/10/24	6944.166	3.110	0.280	3.390	100.742	-24.882
10/11/24	7064.008	3.080	0.230	3.310	100.367	-33.896
10/12/24	6571.037	3.200	0.200	3.400	99.729	-49.198

Table 6.4: Cost And Transfer Times for different phases transfer $L_1 - L_2$

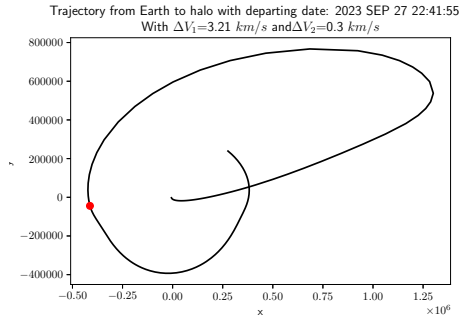

(a) Arrival at halo: 2024 JAN 19 18:17:00

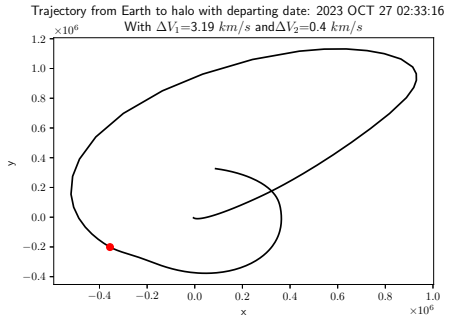

(b) Arrival at halo: 2024 FEB 18 06:50:10

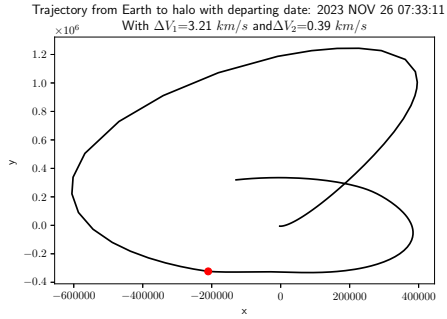

(c) Arrival at halo: 2024 MAR 18 21:33:36

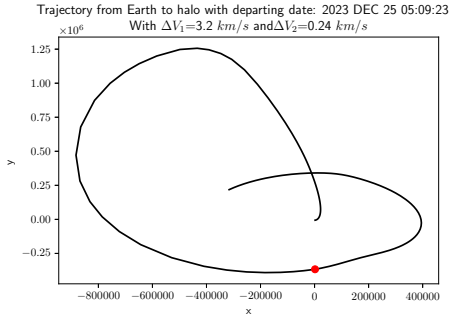

(d) Arrival at halo: 2024 APR 17 14:06:37

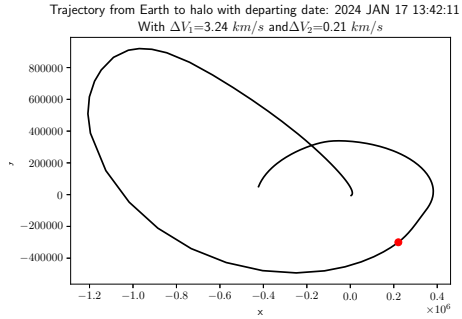

(e) Arrival at halo: 2024 MAY 17 07:45:37

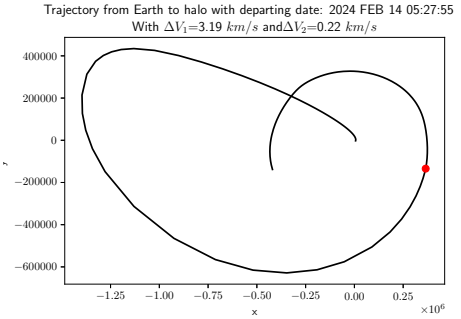

(f) Arrival at halo: 2024 JUN 16 01:27:08

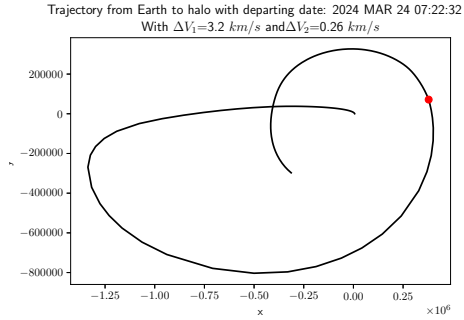

(g) Arrival at halo: 2024 JUL 15 18:05:49

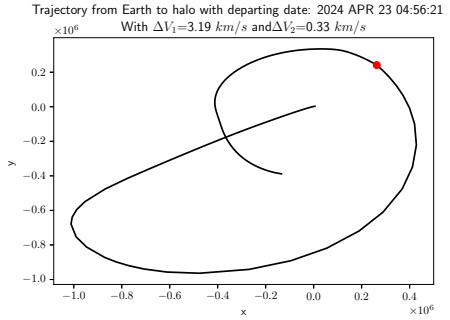

(h) Arrival at halo: 2024 AUG 14 08:58:52

Figure 6.5: Transfer $L_2 - L_2$ comparison between arrival dates, Part 1

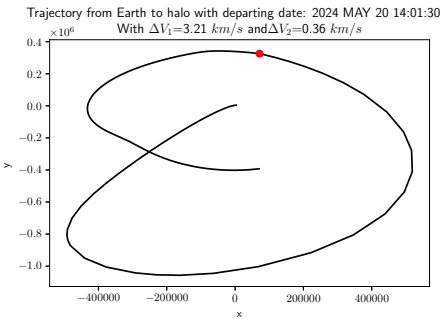

(a) Arrival at halo: 2024 SEP 12 21:56:52

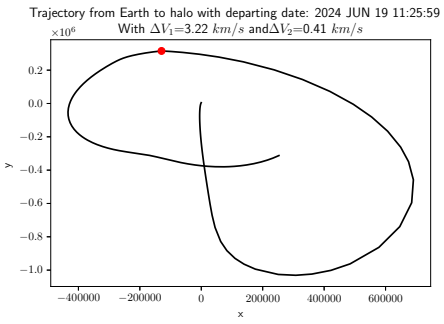

(b) Arrival at halo: 2024 OCT 12 09:14:08

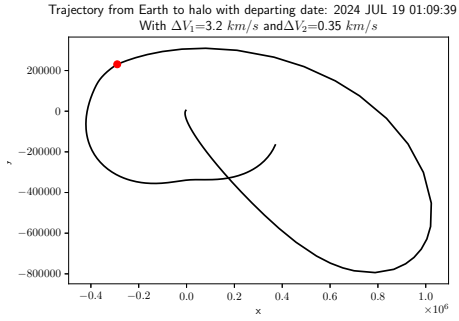

(c) Arrival at halo: 2024 NOV 10 19:11:59

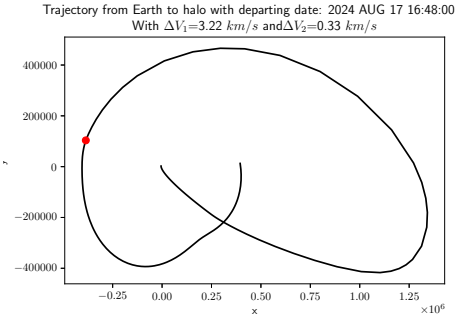

(d) Arrival at halo: 2024 DEC 10 04:10:53

Figure 6.6: Transfer $L_2 - L_2$ comparison between arrival dates, Part 2

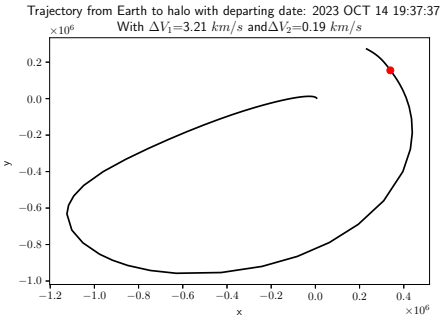

(a) Arrival at halo: 2024 JAN 19 18:17:00

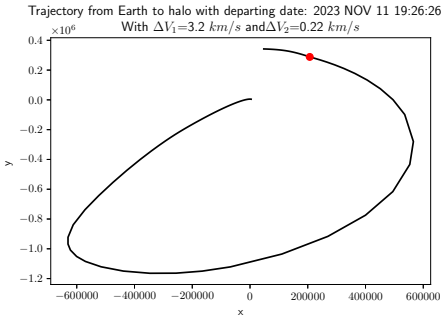

(b) Arrival at halo: 2024 FEB 18 06:50:10

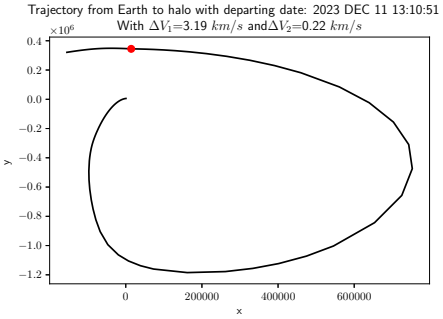

(c) Arrival at halo: 2024 MAR 18 21:33:36

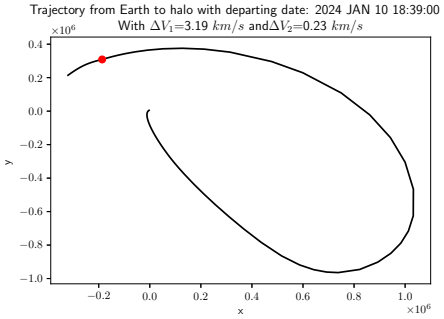

(d) Arrival at halo: 2024 APR 17 14:06:37

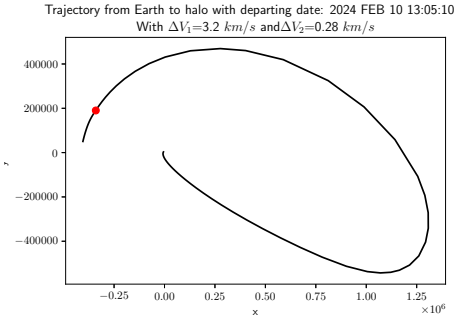

(e) Arrival at halo: 2024 MAY 17 07:45:37

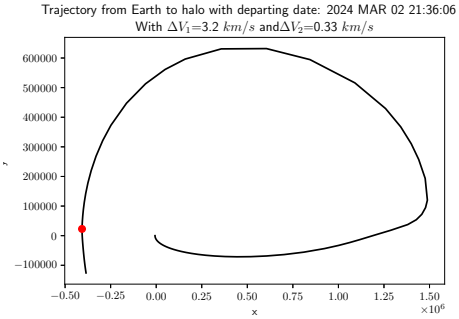

(f) Arrival at halo: 2024 JUN 16 01:27:08

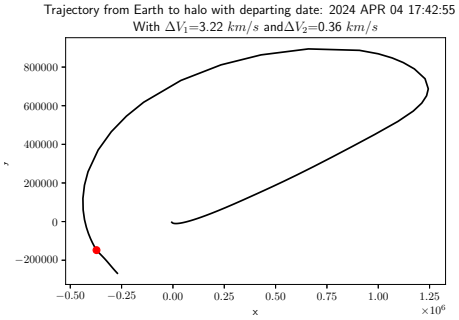

(g) Arrival at halo: 2024 JUL 15 18:05:49

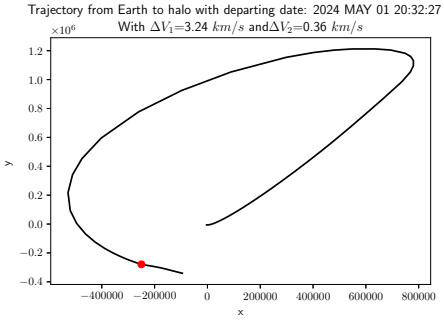

(h) Arrival at halo: 2024 AUG 14 08:58:52

Figure 6.7: Transfer $L_1 - L_2$ comparison between arrival dates, Part 1

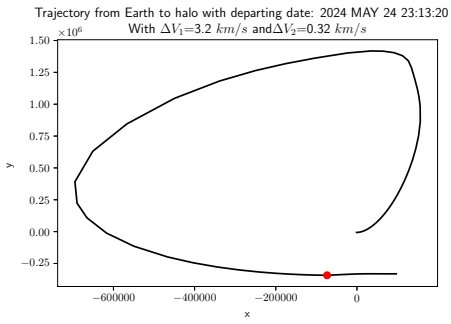

(a) Arrival at halo: 2024 SEP 12 21:56:52

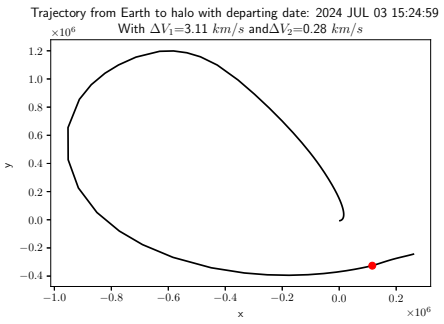

(b) Arrival at halo: 2024 OCT 12 09:14:08

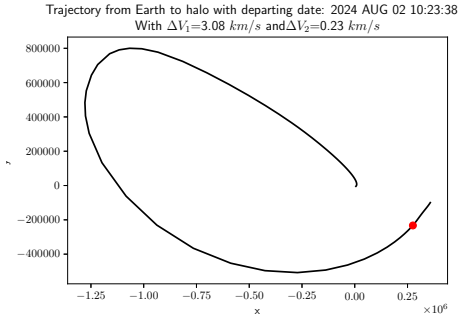

(c) Arrival at halo: 2024 NOV 10 19:11:59

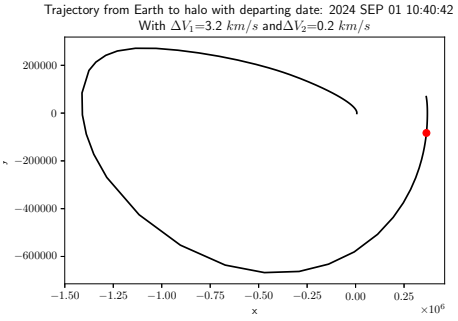

(d) Arrival at halo: 2024 DEC 10 04:10:53

Figure 6.8: Transfer $L_1 - L_2$ comparison between arrival dates, Part 2

6.4 Conclusive Remarks

It has been shown that both trajectories can reduce the transfer cost if compared to the traditional Hohmann transfer. Between $L_2 - L_2$ and $L_1 - L_2$ trajectories the second option is more convenient since the transfer time and cost is lower, but some exceptions are present. For example, if an arrival at halo orbit in July is required, then a $L_2 - L_2$ transfer has a lower cost but maintains a higher travel time. Anyhow, due to the high degree of non linearity in the problem, it is always advisable to test both strategies and it is difficult to make any prevision.

Additionally, the CR3BP models the reality with a good degree of approximation and with the correct margins the ΔV and travel time estimated can be utilised in the preliminary design stages, drastically reducing the computation time required.

6.5 Future Work

This tool provides a preliminary estimate of the transfer cost, with a relatively short computation time. Further refinements can be applied both in the form of better trajectory optimization and of additional constraints, especially in the perturbed trajectory calculation. In particular :

- A fixed time multiple shooting method was implemented. Therefore corresponding nodes in the CR3BP and the ephemerides model may have different position but their time does not vary as well as the transfer time between two consecutive nodes. Allowing for greater flexibility may lead to better solutions or faster convergence.
- Only Earth, Moon and Sun were included as perturbing bodies and no effect of the solar pressure was included. Therefore adding other celestial bodies' contributes and the effect of solar pressure may vary the final trajectory, even though no major variation is expected.
- Only the departing point's altitude is imposed and ΔV is calculated considering a circular parking orbit. Imposing additional constraints could limit the number of available dates or increase the transfer cost, but would allow more control by the user on departure conditions.
- More refined intersection methods for manifolds intersection can be implemented, increasing computational time, but obtaining lower cost transfers, at least in the CR3BP. An example can be found in the Ph.D. dissertation by Elisabet Canalias Vila [26]

Appendix A

Halo Computation

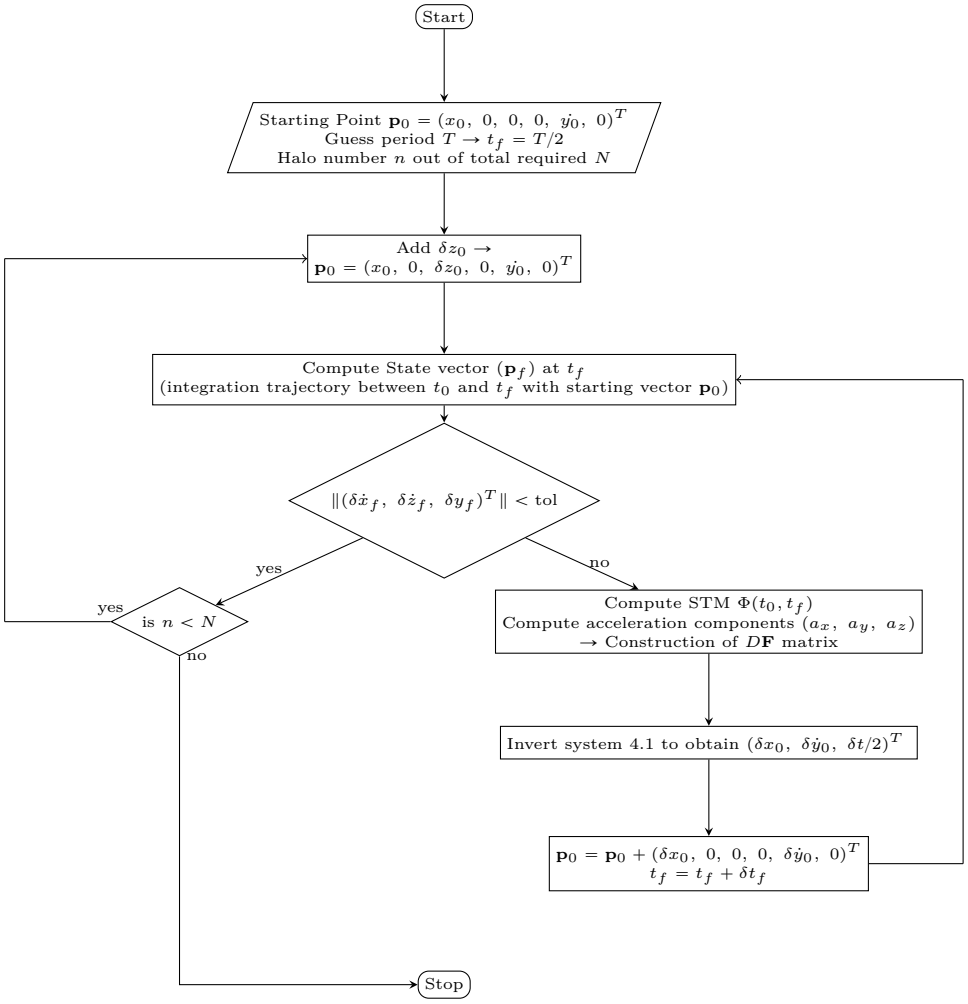

Bibliography

[1] Roger R. Bate, Donald D. Mueller, and Jerry E. White. *Fundamentals of Astrodynamics*. New York: Dover Publications, 1971.

[2] Pooja Dutt, Anilkumar A K, and Raju K George. «Design and analysis of Weak Stability Boundary trajectories to Moon». In: *Astrophysics and Space Science* 363 (July 2018). DOI: 10.1007/s10509-018-3378-y.

[3] Francesco Topputo and Edward Belbruno. «Computation of weak stability boundaries: Sun–Jupiter system». In: *Celestial Mechanics and Dynamical Astronomy* 105 (Nov. 2009), pp. 3–17. DOI: 10.1007/s10569-009-9222-5.

[4] Edward Belbruno. *Weak Stability Boundary and Capture in the Three-Body Problem - Edward Belbruno*. 2011. URL: https://www.youtube.com/watch?v=rp0SAAsY0CY&t=837s&ab_channel=InstituteforAdvancedStudy (visited on 02/09/2022).

[5] Edward Belbruno and J. K. Miller. «Sun-Perturbed Earth-to-Moon Transfers with Ballistic Capture». In: *Journal of Guidance Control and Dynamics* 16 (1993), pp. 770–775.

[6] Ferran Garcia and Gerard Gomez. «A note on weak stability boundaries». In: *Celestial Mechanics and Dynamical Astronomy* 97 (Feb. 2007), pp. 87–100. DOI: 10.1007/s10569-006-9053-6.

[7] ESA. *SMART-1*. 2022. URL: https://www.esa.int/Enabling_Support/Operations/SMART-1 (visited on 02/09/2022).

[8] A.A. Siddiqi and United States. NASA History Program Office. *Beyond Earth: A Chronicle of Deep Space Exploration, 1958-2016*. NASA SP. National Aeronautics and Space Administration, Office of Communications, NASA History Division, 2018. ISBN: 9781626830431. URL: https://books.google.it/books?id=tStkxwEACAAJ.

[9] JAXA. *HITEN*. 2019. URL: https://www.isas.jaxa.jp/en/missions/spacecraft/past/hiten.html (visited on 02/09/2022).

[10] NASA. *GRAIL (Ebb and Flow)*. 2019. URL: https://solarsystem.nasa.gov/missions/grail/in-depth/ (visited on 02/09/2022).

[11] NASA. *GATEWAY*. 2019. URL: https://www.nasa.gov/gateway/overview (visited on 02/09/2022).

[12] Alessandro Benetton. «Design for Lagrangian Points Trajectories. A Complete Force Model Approach». MA thesis. Turin, Italy: Politecnico di Torino, 2018.

[13] Shane Ross et al. *Dynamical Systems, the Three-Body Problem, and Space Mission Design*. Apr. 2011. ISBN: 978-0-615-24095-4.

[14] Elisa Maria Alessi. «The role and Usage of Libration Point Orbits in the Earth- Moon system». MA thesis. Barcelona, Spain: Universitat de Barcelona, 2010.

[15] Edward Belbruno, Marian Gidea, and Francesco Topputo. «Weak Stability Boundary and Invariant Manifolds». In: *SIAM J. Applied Dynamical Systems* 9 (Jan. 2010), pp. 1061–1089. DOI: 10.1137/090780638.

[16] Prof. Jerrold E. Marsden. *Lecture notes in Introduction to Dynamical Systems*. 2009.

[17] Victor G. Szebehely and F. T. Geyling. «Theory of Orbits: The Restricted Problem of Three Bodies». In: 1967.

[18] Wikipedia. *Poincaré map*. 2022. URL: https://en.wikipedia.org/wiki/Poincar\%C3\%A9_map (visited on 02/09/2022).

[19] The SciPy community. *scipy.integrate.solve_ivp*. 2008. URL: https://scipy.github.io/devdocs/reference/generated/scipy.integrate.solve_ivp.html?highlight=solve_ivp#r179348322575-14 (visited on 02/07/2022).

[20] Davide Guzzetti et al. «STATIONKEEPING ANALYSIS FOR SPACECRAFT IN LUNAR NEAR RECTILINEAR HALO ORBITS». In: Feb. 2017.

[21] The SciPy community. *scipy.optimize.fmin*. 2008. URL: https://scipy.github.io/devdocs/reference/generated/scipy.optimize.fmin.html?highlight=fmin#scipy.optimize.fmin (visited on 02/07/2022).

[22] Han-qing Zhang and Yan-jun Li. «The design of Earth-Moon transfer trajectory using Sun-Earth L1 libration point manifolds». In: *2011 3rd International Conference on Advanced Computer Control*. 2011, pp. 417–421. DOI: 10.1109/ICACC.2011.6016444.

[23] Wikipedia. *Ephemeris*. 2022. URL: https://en.wikipedia.org/wiki/Ephemeris (visited on 02/08/2022).

[24] NAIF. *About SPICE*. 2022. URL: https://naif.jpl.nasa.gov/naif/spiceconcept.html (visited on 02/08/2022).

[25] NAIF. *NAIF CSPICE Toolkit Hypertext Documentation*. 2022. URL: https://naif.jpl.nasa.gov/naif/aboutspice.html (visited on 02/08/2022).

[26] Elisabet Canalias Vila. «Contributions to Libration Orbit Mission Design using Hyperbolic Invariant Manifolds». PhD thesis. Barcellona: Universitat Politecnica de Catalunya, May 2007.